Biophysical Journal
Article

Biophysical Society

Dynamics of Mechanosensitive Nascent Adhesion Formation

Laurent MacKay[1] and Anmar Khadra[1,*]
[1]Department of Physiology, McGill University, Montreal, Quebec, Canada

ABSTRACT Cellular migration is a tightly regulated process that involves actin cytoskeleton, adaptor proteins, and integrin receptors. Forces are transmitted extracellularly through protein complexes of these molecules, called adhesions. Adhesions anchor the cell to its substrate, allowing it to migrate. In Chinese hamster ovary cells, three classes of adhesion can be identified: nascent adhesions (NAs), focal complexes, and focal adhesions, ranked here ascendingly based on size and stability. To understand the dynamics and mechanosensitive properties of NAs, a biophysical model of these NAs as colocalized clusters of integrins and adaptor proteins is developed. The model is then analyzed to characterize the dependence of NA area on biophysical parameters that regulate the number of integrins and adaptor proteins within NAs through a mechanosensitive coaggregation mechanism. Our results reveal that NA formation is triggered beyond a threshold of adaptor protein, integrin, or extracellular ligand densities, with these three factors listed in descending order of their relative influence on NA area. Further analysis of the model also reveals that an increase in coaggregation or reductions in integrin mobility inside the adhesion potentiate NA formation. By extending the model to consider the mechanosensitivity of the integrin bond, we identify mechanical stress, rather than mechanical load, as a permissive mechanical parameter that allows for noise-dependent and independent NA assembly, despite both parameters producing a bistable switch possessing a hysteresis. Stochastic simulations of the model confirm these results computationally. This study thus provides insight into the mechanical conditions defining NA dynamics.

SIGNIFICANCE This manuscript makes valuable contributions in deciphering the dynamics of nascent adhesions (NAs). It presents a novel mathematical model that determines how mechanical stress applied to these adhesions governs their assembly and disassembly. The model is biophysically relevant; it provides a framework that links NA area to the number of mobile or immobile integrins along with adaptor proteins and considers a multitude of experimental observations defining their mechanosensitive properties. The model is then examined to uncover how four components of this systems interact: NA area, integrin and adaptor proteins coaggregation, number of integrins and adaptor proteins within NAs, and force exerted on NAs. It is the first study that uniquely identifies adhesion stress, rather than its total load, as the mechanical parameter conserved during NA formation.

INTRODUCTION

Cellular migration plays a fundamental role in many physiological and pathophysiological systems, including embryonic morphogenesis and continual tissue regeneration (1), immune responses (2), tissue repair (3), and the metastatic properties of cancers (4). Typically, cellular migration occurs in response to an extracellular signal in the form of a chemical or mechanical gradient (5,6), leading to cellular polarization through nonlinear processes governing biochemical pathways that internally amplify the extracellular gradients to establish a front and rear of the cell (7,8). Cells attach themselves to their external environment by forming integrin-based adhesion complexes that anchor to the substrate and act as an extension of the cytoskeleton. This results in an active remodeling of the cytoskeleton and causes a net displacement of the cell along the substrate (9,10).

Adhesions serve as a point of force transmission to the external environment for motile cells. This force transmission is primarily mediated through integrin receptors, which span the cellular membrane and bind to their extracellular ligands (e.g., collagen and fibronectin). They form partially immobilized traction points that a cell can use to move itself or to deform the external environment. The cytoplasmic domains of integrins are linked to the actin cytoskeleton

Submitted January 30, 2019, and accepted for publication August 2, 2019.
*Correspondence: anmar.khadra@mcgill.ca
Editor: Vivek Shenoy.
https://doi.org/10.1016/j.bpj.2019.08.004

through a variety of adaptor proteins that interact through biochemical signaling pathways (11–13), creating a biologically regulated mechanical coupling system that links the actin cytoskeleton with the extracellular matrix (ECM). The interactions between these proteins, along with mechanical forces arising from active processes in the cytoskeleton, establish complex spatiotemporal patterns of activity (7,8). These patterns regulate the dynamics of adhesion assembly and disassembly (14,15) and cytoskeletal organization (9,16,17), producing cellular migration in response to extracellular cues (10).

Adhesions are formed in a stepwise manner, starting as nascent adhesions (NAs), a class of dynamic nanoscale clusters of integrin receptors (referred to hereafter as integrins) that contain on average 20–50 integrins (18,19). Many mechanisms, such as increases in the long-range lateral mobility of integrins (e.g., reduced corralling by actin cytoskeleton), local changes in their free diffusivity, and modulation of their binding affinity through interactions with the adaptor protein talin, have been found to be relevant in the formation and regulation of integrin clusters (20–26). Experimentally dissecting the effect of each mechanism on adhesion formation has often been obscured by the fact that all these effects are simultaneously present in physiological conditions (21,24,27). Theoretical models of adhesions allow for independent modulation of these mechanisms to study their effects. Existing models of adhesions either have idealized their physical model of an adhesion (10,28–31) or have focused on certain phenomenological aspects of the system (30,32–34) that are not applicable during the formation of NAs. Others are more biologically realistic with many variables, making it difficult to understand the underlying dynamics (35–41).

Integrins are intrinsically mechanosensitive, capable of exhibiting a catch-bond behavior (42). In contrast to the more common slip bonds (43), catch bonds exhibit a nonmonotonic profile in their lifetime when plotted as a function of the applied force. This profile suggests that there exists a nonzero optimal applied force that maximizes the bond lifetime, for which the increase in bond lifetime is associated with a conformational change to a long-lived bound state (44,45). It has been proposed that this phenomenon may reflect the activation of integrins (i.e., the induction of a high-affinity bound state) by mechanical forces (45,46). Because of their position in the mechanical linkage between the cell and its environment, the mechanosensitivity of integrins is likely to be implicated in adhesion dynamics. This has been investigated thoroughly from a theoretical perspective by considering a finite number of bonds that may rupture because of force and rebinding (28,29,34,47). These studies have reported disassembly of clusters of bonds but have not yet examined how assembly is manifested in the presence of applied force. Thus, determining the effect(s) of force on NA dynamics during assembly and disassembly remains incomplete.

The process of adhesion assembly into a cluster containing tens of molecules starting from a single molecular-complex initial condition (e.g., a single integrin-adaptor protein complex) was previously demonstrated through stochastic simulations of a molecular model that considered many possible state transitions (41). However, mean-field analysis of this molecular model was performed using a simplified one-variable ordinary differential equation (ODE) model, predicting an unstable steady state that blocks the assembly of very small adhesions (41). In theory, it should be possible to jump over this unstable state because of stochastic effects even in one dimension. However, the conditions necessary to produce such a jump remain unexplored. Moreover, other studies that produce similar configurations of steady states also predict a net loss in both the number of bound integrins and adaptor proteins when adhesions are very small (39,40,47). On the one hand, this is congruent with the proposition that NAs are thermodynamically unfavorable structures and thus are the product of stochastic fluctuations (30,48,49). On the other hand, NAs have been shown to be stable for hundreds of seconds in appropriate mechanical conditions, suggesting that they are, in fact, thermodynamically favorable structures (18,49). To further investigate this, we develop here a mathematical model that possesses an elevated equilibrium representing NAs that can either 1) allow for NA assembly independently of stochastic effects or 2) be used to understand in more detail the conditions required for noise-induced NA formation.

Because of the limited understanding of NA assembly dynamics, we present in this study this biophysically based mathematical model of NA formation and stabilization, which considers a multitude of experimental observations and provides precise characterization of their underlying behavior in various conditions. We then use the model, which not only considers the integrin bonds but also the adhesion plaque formed by adaptor proteins, to demonstrate how assembly and disassembly are affected by force and their dynamics are manifested under various physiologically relevant contexts.

METHODS

Mathematical model of NA formation

We propose a biophysical model of NA formation based on a mechanism we term coaggregation, in which the interaction of integrins in the membrane with adaptor proteins in the cytoplasm leads to the colocalized aggregation of both into discrete structures (see Supporting Materials and Methods for a detailed derivation of the model). This model is constructed to incorporate a number of experimental observations:

O1. NAs have a circular geometry, and they grow isotropically (50). This is in contrast to the growth of larger and typically elongated focal adhesions, which is highly anisotropic (48,50).

O2. Adaptor proteins exhibit a wide range of mobilities that vary in a location-dependent manner.

(a) Adaptor proteins diffuse rapidly in the cytosol, whereas they diffuse more slowly inside adhesions (51).

(b) Their mobility within adhesions is highly heterogeneous, suggesting that they exist in more than one state in the adhesion plaque (52,53).
(c) Some adaptor proteins have a longer residency time in adhesions containing a higher density of integrins, suggesting that a reduction in adaptor mobility is due to interactions (binding or tethering) with integrin (54).

O3. Integrins diffuse laterally along the membrane. Their free diffusion is slower within the adhesion, and this effect is likely due to interactions with adaptor proteins on the cytoplasmic side of the membrane (25).
O4. Integrins become immobilized for extended periods of time upon binding to ligand, and this process is favored inside adhesions (55).
O5. The integrin-ligand bond lifetime varies with force (42), exhibiting a biphasic profile with a maximal value at nonzero applied force (~37 pN).

Furthermore, in the derivation of model equations, we have also made a number of assumptions that are primarily based on experimental observations:

M1. As suggested in O1, the model defines an NA as a two-dimensional region of space on the membrane demarcated by the boundary of a membrane-proximal circular adhesion plaque with area A (see Fig. 1).
M2. The adhesion plaque is a condensed phase of interacting adaptor proteins tethered to the membrane by integrins. Adaptor proteins are assumed to be incorporated with a fixed density through adsorption. The density, ρ, is determined by the mean volume of all adaptor proteins in the plaque, and the length of the bonds between them.
(a) According to O2a, we assume that the cytoplasmic pool of adaptor proteins is well-mixed (see Eq. S6), whereas adaptor proteins in the adhesion plaque exhibit reduced mobility because of interactions with other adaptor proteins in the plaque and integrins in the membrane.
(b) The adhesion-plaque dynamics are derived based on the assumption that it can grow or shrink because of the adsorption or loss of adaptor proteins to or from any point in its interior, respectively; this assumption corresponds to the "bulk-on/bulk-off" formalism considered previously (30). The choice of this formalism is motivated by the notion that NAs are not strongly associated with the actin cytoskeleton during their assembly (56,57), allowing for the adsorption or loss of adaptor proteins through the dorsal face of the adhesion. This assumption would not be appropriate for models dealing with the maturation of NAs, as that process seems to be intrinsically tied to an increased association with organized actin filaments (50,56,58) that protect the adhesion from degradation by loss of matter through its dorsal face (30).
(c) From O2b and O2c, the multiple mobility states of adaptor proteins in the adhesion are interpreted as being due to their tethering to the membrane by integrin receptors (i.e., in a state with lower mobility if the adaptor protein is tethered to the membrane but in a state with higher mobility if it is only associated with other adaptor proteins). This implies that a nonlinear relation between the adhesion's disassembly rate and its integrin content exists (see Eq. S7).
M3. Underneath the adhesion plaque, there are a total of N_{in} integrins. L_{in} of these integrins are liganded and immobilized while M_{in} are mobile and diffuse freely (i.e., $N_{in} = L_{in} + M_{in}$; see Fig. 1).
(a) Per O3, we use a position-dependent diffusion coefficient to abruptly change the diffusivity of integrins from D_{out} to D_{in} when they pass from the outside to the inside of the adhesion ($D_{out} > D_{in}$; see Eq. S2).
(b) Per O4, integrins inside the adhesion bind to their ligands with a rate k_{bind}. Furthermore, we assume that bound integrins are completely immobile. To account for the density of extracellular ligand, we take the binding rate to be proportional to ligand density (i.e., $k_{bind} = \bar{k}_{bind}[\text{Ligand}]$).
(c) Per O5, bound integrins inside the adhesion unbind from their ligands with a rate $k_{unbind}(f)$, where f is the force applied to a single integrin (see Eq. S14 for details on the form of $k_{unbind}(f)$ and assumption M4a for the determination of f). Bound integrins outside the adhesion unbind with a rate $k_{unbind}(0)$, with this situation only occurring when the adhesion plaque is shrinking.
M4. The total load applied to the adhesion is distributed evenly among all bound integrins. Therefore, when an integrin unbinds, the load is distributed over the (fewer) remaining bound integrins such that each receptor feels an increase in applied force.
(a) The force, f, applied to each integrin is computed by assuming that the NA is under fixed stress, $\sigma = (fL_{in}/A)$, and that each bound integrin bears an equal load (see Eq. S17).

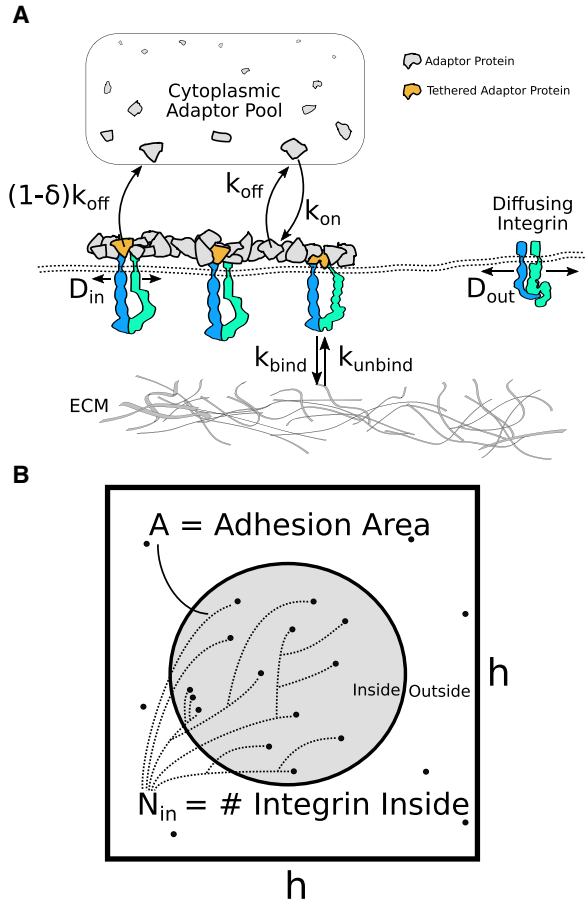

FIGURE 1 Schematic of the model describing adhesion formation. (*A*) Integrins and adaptor proteins coaggregate to form a membrane-proximal adhesion plaque, under which sits a cluster of integrins that exhibit a decreased diffusion coefficient ($D_{in} \leq D_{out}$) and become immobilized upon binding to ligand. Adaptor proteins that are in the proximity of integrins are assumed to be reversibly tethered to the membrane. Untethered adaptor proteins leave the plaque with a rate k_{off}, whereas tethered ones leave at a rate $(1-\delta)k_{off}$. (*B*) Geometry of the $h \times h$-square lattice containing the adhesion domain Ω is shown. NAs possess a circular geometry confined to grow in this square lattice cell. The area of the adhesion plaque ($A(t)$) and the number of integrins it contains ($N_{in}(t)$) are dynamic variables that vary because of adsorption and diffusion, respectively. To see this figure in color, go online.

M5. For simplicity, we consider a periodic square lattice of adhesions with an interadhesion spacing of h (see Fig. 1). The flux of matter between the square lattices is at equilibrium and thus the total matter in each square is assumed to be conserved. Model parameters are chosen in such a way that to prevent the adhesion from extending beyond the dimension of a single lattice cell (see Geometric Constraints).

Mathematically, the coaggregation mechanism discussed above is implemented through the interaction of the integrin-dependent tethering mechanism (M2c) and the reduced integrin mobility inside the adhesions (M3a and M3b).

The behavior of the model is investigated through two complementary approaches: 1) by investigating its full spatiotemporal dynamics using stochastic simulations and 2) by characterizing the outcomes of the stochastic simulations using a simplified differential equation model of NAs describing the dynamics near equilibrium. The simplified model is given by the following set of ODEs:

$$\dot{A} = A\left[\underbrace{\left(k_{on}^{0}\left(\frac{C_P}{\rho}-\frac{A}{h^2}\right)\right)}_{\text{Plaque growth}} - \underbrace{k_{off}\left((1-\delta)+\delta\frac{b^n}{b^n+\left(\frac{M_{in}+L_{in}}{A}\right)^n}\right)}_{\text{Plaque shrinking}}\right], \tag{1a}$$

$$\dot{M}_{in} = \underbrace{2\sqrt{\pi A}\left(\frac{D_{out}(C_I h^2 - M_{in} - L_{in})}{h^2 - A} - \frac{D_{in}M_{in}}{A}\right)}_{\text{Mobile integrin net diffusion}} - \underbrace{(k_{bind}M_{in} - k_{unbind}(f)L_{in})}_{\text{Integrin}-\text{ligand binding kinetics}}, \tag{1b}$$

$$\dot{L}_{in} = k_{bind}M_{in} - k_{unbind}(f)L_{in}, \tag{1c}$$

where k_{on}^{0} is a kinetic parameter related to the rate of adsorption of adaptor proteins into the adhesion (see Parameter Estimation for more details), k_{off} is the off-rate of adaptor proteins from the adhesion in the absence of integrins, δ is the fractional reduction in the off-rate of adaptor proteins when tethered to the membrane by integrins, b is the concentration of integrin inside the adhesion that results in the tethering of 50% of adaptor proteins in the adhesion plaque, n is the degree of cooperativity between integrins for the tethering of adaptor proteins, and C_I (C_P) is the mean density of integrins (adaptor proteins) taken by averaging over the $h \times h$ lattice cell. For detailed description and derivation of the model, see Supporting Materials and Methods.

Conditional expectation analysis

We have developed a computational method to infer the conditional mean of one physical variable given the value of another dependent physical variable. This technique is used to assess the relation between NA area, A, and the number of integrins it contains, N_{in}, by using only the two terms P_A and $P_{N_{in}}$, representing the marginal distributions of these quantities, respectively. Briefly, we assume $A = f(\overline{N}_{in}) = \mathbb{E}(A \mid N_{in})$, where $\mathbb{E}(x \mid y)$ denotes the conditional expectation of the variable x given the value of another variable y, and then use Bayesian methods to quantitatively estimate $f(\bullet)$using the change-of-variable formula given by $P_A = P_{N_{in}}/f'(N_{in})$. See Supporting Materials and Methods for further details.

Model parameters

We have used a complex systems approach to parameter determination, applying different estimation techniques to guarantee that our model produces predictions that are consistent with experimental findings while also exhibiting the emergent behavior of the system under consideration (i.e., NAs). This is accomplished by deriving analytical expressions (e.g., steady states of the model) that can be equated to experimental measurements (18,25,42,51) and then solving the resulting set of nonlinear equations to quantify model parameters. This approach is used to determine the parameters b, h, C_I, $K_{in} = D_{out}/D_{in}$, $K_{on} = k_{on}^{0}/k_{off}$, and $K_{bind} = k_{bind}/k_{unbind}$. Furthermore, the previously published data describing the distributions of protein cluster sizes and number of integrins within these protein clusters (18) are digitized and utilized to derive a relation between A and N_{in} using conditional expectation analysis (described above). The nonzero A-nullcline, obtained by setting Eq. 1a to zero while assuming no cooperativity (i.e., by letting $n = 1$), is then fitted to this relation using a nonlinear least-squares fitting procedure that yields estimates for the two identifiable parameters

$$A_0 = h^2\left(\frac{C_P}{\rho} - \frac{1}{K_{on}}\right)$$

and

$$A^{\infty} = h^2\left(\frac{C_P}{\rho} - \frac{1-\delta}{K_{on}}\right).$$

Estimating these identifiable parameters is necessary to determine the values of b and K_{on} (see Supporting Materials and Methods). The parameters δ, D_{out}, k_{unbind}, and C_P are estimated directly from experimental data (25,42,55,59). Finally, the remaining two parameters k_{off} (or k_{on}^{0}) and ρ are manually tuned to obtain stochastic simulations that are comparable

to experimental recordings of adhesion assembly and disassembly (50). Parameter values are used to explain how the analytical results of our model manifest themselves numerically when constrained by experimental data. The qualitative behavior of the model does not depend critically on parameter choices made; this is to be expected because almost all results presented here have been obtained analytically. For more details about parameter estimation, see Supporting Materials and Methods.

Software

Stability analysis for fixed protein density and binding affinity is performed symbolically using Mathematica Version 11.3 (Wolfram Research, Champaign, IL). On the other hand, for fixed adhesion stress, stability analysis is conducted numerically using the continuation software AUTO-07p to obtain the location of bifurcation points (60), The stability of branches obtained are then cross-validated using Mathematica and MATLAB (The MathWorks, Natick, MA). Stochastic simulations and nonlinear least-squares fitting are performed using MATLAB. Parameter estimation is also done using Mathematica. The code used for ODE analysis, numerical continuation, and stochastic simulations can be obtained online (61).

RESULTS

The relation between NA area and its integrin content

To understand NA dynamics, we first aim to establish how their area and integrin content are related. If this relation is linear, then the density of integrins inside the adhesion is constant, and the area of the adhesion can be explained by N_{in} alone. Such a relation could be used to estimate the effective membrane area of a single integrin and motivates the theoretical assumption of a fixed ratio of integrin/adaptor proteins (32–34,36). If this relation is nonlinear, on the other hand, then the area of the adhesion cannot be explained solely by the number of integrins and their physical dimensions. In such a case, it would be inaccurate to use models that assume a fixed ratio of integrin/adaptor proteins.

To investigate this, we have digitized previously published distributions of NA diameter and their integrin content (18). The distribution of NA diameter is first converted to a distribution of NA area A by assuming a circular geometry, followed by applying conditional expectation analysis (see Methods) to quantify the relation between the two random variables A and N_{in}. This analysis is motivated by the significant differences in skewness between the distributions, suggesting the possibility of a nonlinear relation. Indeed, our results (see Fig. 2 *A*) reveal that this relation appears to have a saturating "sigmoidal" phase for NAs containing up to ~190 integrins, followed by a linear phase for larger adhesions. This indicates that the integrin density inside the adhesion, N_{in}/A, is not fixed in small NAs (see *dotted line* in Fig. 2 *B*), and therefore, the size of these NAs cannot be explained by the number of integrins it contains. This sigmoid relation thus must be taken into consideration when formulating the model for NAs.

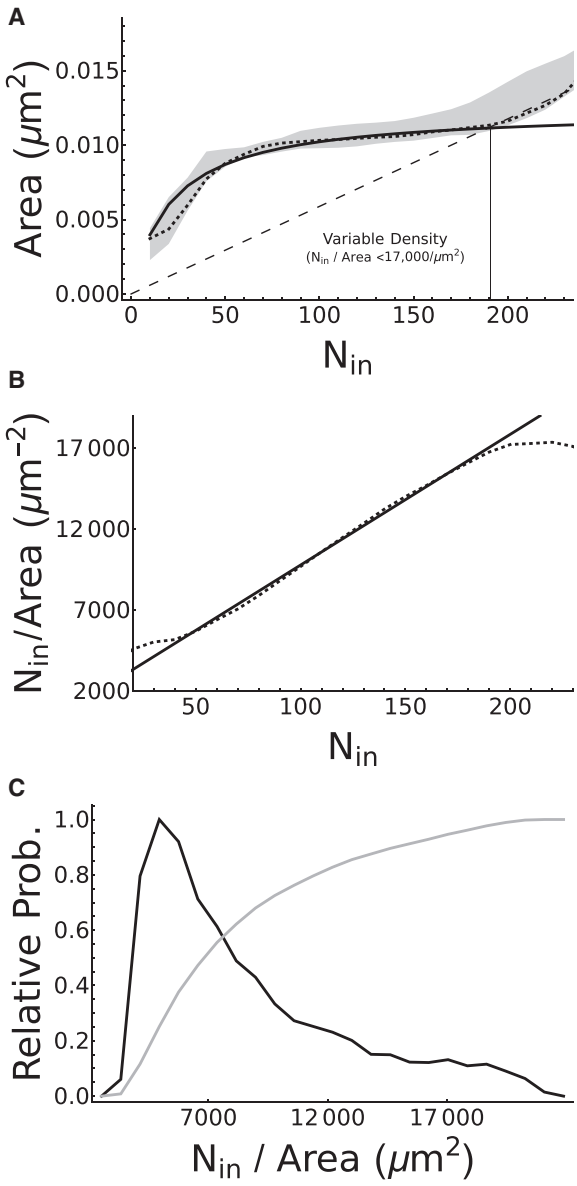

FIGURE 2 (*A*) Inferred relation between NA area A and its integrin content N_{in} as determined by conditional expectation analysis. Bayesian inference is used to determine an empirical relation between A and N_{in} under the assumption that NAs are circular. After digitizing the distributions of NA diameters and their integrin contents published in (18), a relation between them is quantified. A 99.95% confidence interval is plotted in gray, demonstrating that the data generally exhibits a nonlinear relation between the two variables. The maximal a posteriori (MAP) estimate of this relation is also plotted as a dotted line, suggesting that NA area depends sigmoidally on N_{in} for small adhesions, whereas this dependence is linear for large adhesions (compare to *dashed line*). The nontrivial A-nullcline of the model, describing the relation between the two variables near equilibrium as defined by Eq. 2 (*solid line*), is fitted to the MAP estimate in the nonlinear phase and found to be in agreement. (*B*) The computed integrin density inside the adhesion, $N_{in}/A(N_{in})$, is given. Estimates are computed from the data-derived MAP estimate of $A(N_{in})$ (*dotted line*) and from the model prediction for $A(N_{in})$ given by Eq. 2 (*solid line*). Both curves exhibit a linear increase in integrin density with respect to N_{in} for $N_{in} \in [50, 190]$. (*C*) The probability distribution of integrin densities is shown. Black line: probability density function $P(N_{in}/A) = P(N_{in})[d(N_{in}/A(N_{in}))/dN_{in}]^{-1}$, where $A(N_{in})$ is given by Eq. 2; gray line: cumulative density function.

To account for this, we have incorporated assumption M2c into the model. By setting the left-hand side of Eq. 1a to zero, we solve for the nonzero A-nullcline. This is equivalent to assuming that the observed differences in NA area are due to local variations in integrin availability (i.e., differences in C_I). For simplicity, we consider the absence of cooperativity between integrins in the tethering of adaptor proteins ($n = 1$). The resulting expression for the A-nullcline is given by

$$A(N_{in}) = \frac{(4A^{\infty} bN_{in} + (N_{in} - A_0 b))^{1/2} - (N_{in} - A_0 b)}{2b}, \quad (2)$$

where $A_0 = h^2[(C_P/\rho) - (1/K_{on})]$ is the (possibly negative) area of the adhesion plaque in the absence of coaggregation (i.e., when $\delta \to 0$) with $K_{on} = k_{on}^0/k_{off}$ and $A^{\infty} = h^2[(C_P/\rho) - (1 - \delta)/K_{on}]$ is the maximal area of the adhesion plaque (attained when the mean integrin density in the membrane is arbitrarily high; see Geometric Constraints). The shape of the curve described by Eq. 2. is in agreement with the profile of the relation inferred by conditional expectation analysis (*solid line* in Fig. 2 *A*), supporting the hypothesis that the aforementioned variation in integrin density (inside NAs) may be explained by the tethering mechanism used to formulate Eq. 1a.

We note that the model suggests that integrin density may grow unboundedly (see *solid line* in Fig. 2 *B*), which is due to the treatment of integrins as infinitesimally small point particles. In reality, the physical size of the integrins will eventually have non-negligible effects on their flux as the adhesion becomes increasingly crowded with integrins. Our data analysis demonstrates that adhesions containing integrin densities up to $\sim$17,000 μm^{-2} are not strongly influenced by these molecular crowding effects, as can be seen from the saturating relation between A and N_{in} for $N_{in} < 190$. Conversely, above this threshold in density, we have $A \propto N_{in}$, suggesting that the crowding of integrins plays a significant role in determining the size of larger adhesions.

The maximal integrin density we have computed is significantly higher than the mean densities of $\sim$1000 μm^{-2} previously reported in Wiseman et al. (62), or the $\sim$6600 μm^{-2} computed by Changede et al. (18). Firstly, we would like to note that the most likely integrin density according to our analysis is $\sim$4940 μm^{-2} (see *black line* in Fig. 2 *C*), which is comparable to the value reported by Changede et al. Secondly, it has been previously suggested that Wiseman et al. (62) estimated the mean density of integrins on the membrane because their diffraction-limited imaging would not allow for proper resolution of NA boundaries (18). As such, we note that the value we have used for the mean density of integrins, $C_I = 1844$ μm^{-2}, is comparable to what was reported by Wiseman et al. (62) (see Parameter Estimation for more details).

Furthermore, our approach quantifies the variability of integrin density inside adhesion. Therefore, although our analysis suggests that this density may go as high as $\sim$17,000 μm^{-2}, it also predicts that 80% of adhesions have an integrin density that is less than 12,000 μm^{-2} (see *gray line* in Fig. 2 *C*). Changede et al. (18) previously computed a maximal theoretical density of $\sim$25,000 μm^{-2} based on an estimated integrin footprint of 40 nm^2. Using a hypothetical model (63) built from multiple partial crystal structures of integrin (64–67), we estimate a rectangular bounding box footprint of 7.6 nm $\times$ 4.5 nm $\approx$ 34 nm^2 and 12 nm $\times$ 5 nm $\approx$ 60 nm^2 for the closed and open conformations of integrin, respectively. This provides us with corresponding bounds on the maximal possible density of integrins, given by 29,400 and 16,667 μm^{-2}, respectively. Interestingly, our estimate of 17,000 only marginally surpasses the lower bound on the theoretical maximal density (i.e., when all integrins are in the open conformation) and remains well below the upper bound. This suggests that the majority of the integrins within these high-density NAs are in a closed conformation.

In this study, we focus our analysis on the nonlinear regime identified for $N_{in} < 190$ because NAs typically have $N_{in} \in [20, 50]$ (19). In what follows, we examine the chemical and mechanical regulation of this sigmoidal relation between NA areas and their integrin content through the biophysical parameters, which control both N_{in} and Eq. 2.

Stabilization of the adhesion plaque by integrin

One of the equilibria of Eqs. 1a, 1b, and 1c is the unclustered steady state $(A, M_{in}, L_{in}) = (0, 0, 0)$. The stability of this steady state depends on the values of model parameters. To reduce the complexity of our analysis, we will first consider the model in the absence of force ($f = 0$). In subsequent sections, we will extend our steady-state analysis to include force and then investigate the time course of the model under applied force.

By analyzing the stability conditions of this steady state, we find that it becomes unstable once model parameters cross a threshold (see Supporting Materials and Methods); we will now demonstrate how this corresponds to the induction of adhesion formation. Given that the existence of the unclustered steady state (0, 0, 0) is independent of the degree of cooperativity n, we first restrict our analysis to the case when $n = 1$ for simplicity. This will allow us to build intuition about the behavior of the system and determine what happens for $n > 1$. Under these conditions, the unclustered steady state loses stability through a transcritical bifurcation occurring whenever $C_I > C_I^{\ddagger}$, $C_P > C_P^{\ddagger}$, or [Ligand] $>$ [Ligand]‡ (see Eqs. S11–S13). That is, once there are enough integrins, adaptor proteins, or ligands at the interface between the cell and its environment, the unclustered steady state

becomes unstable, and stable adhesion plaques form (see Fig. 3). This transition occurs when the system undergoes a transcritical bifurcation (see Fig. 3, *A–C*), forming a stable nontrivial steady state, given by

$$A^* = \frac{h^2\left(\Gamma\left(\widehat{C}_I\right) - \widehat{C}_I + b\beta(\phi K_{on} - \delta)\right)}{2b\beta K_{on}}, \quad (3)$$

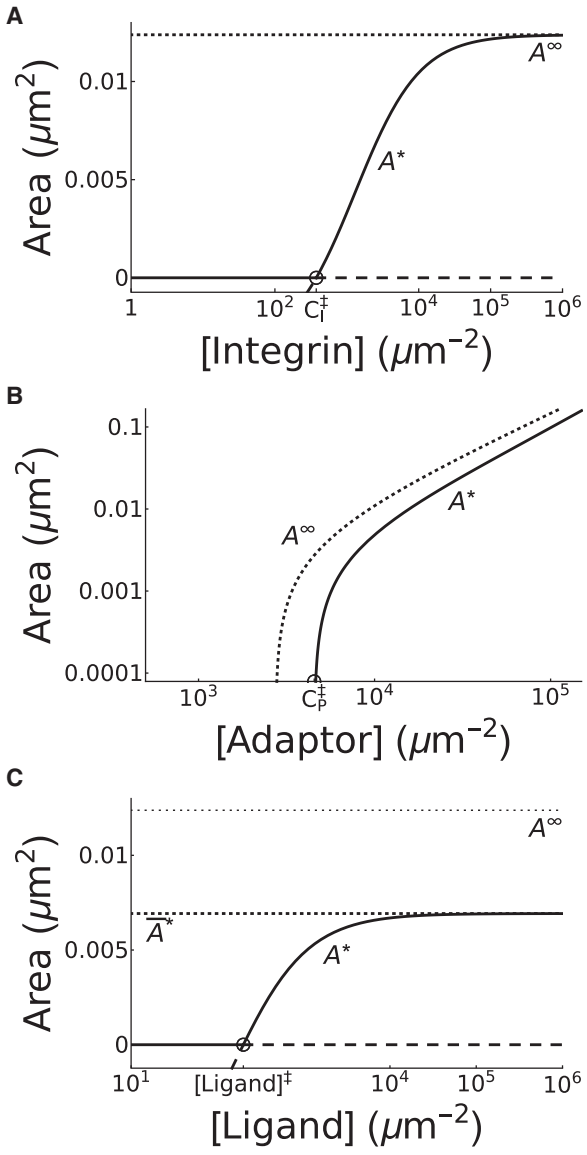

FIGURE 3 Effects of coaggregation on NA area. Bifurcation diagrams of equilibrium adhesion area A^* with respect to (*A*) C_I, (*B*) C_P, and (*C*) [Ligand] are given, showing branches of stable (*solid lines*) and unstable (*dashed lines*) steady states separated by thresholds defined by transcritical bifurcation points (*open circles*). The bifurcation points occur when $C_I = C_I^\ddagger$ in (*A*), $C_P = C_P^\ddagger$ in (*B*), and [Ligand] = [Ligand]‡ in (*C*). The stable branches represent the (un)clustered steady states (before) after the threshold. Notice that increasing C_I leads to a saturating response, eventually plateauing at A^∞ (*dotted line* in *A*), whereas increasing C_P leads to an unbounded growth in adhesion area (*B*). Increasing [Ligand] also produces a saturating response, plateauing at $\overline{A}^* < A^\infty$ (*C*).

$$M_{in}^* = \frac{h^2\left((2\beta\phi + 1)\widehat{C}_I - \Gamma\left(\widehat{C}_I\right) + b(\omega - \beta\delta)\right)}{2\beta(K_{bind} + 1)\omega}, \quad (4)$$

where $\hat{C}_I = (1 + K_{bind})K_{in}K_{on}C_I$, $K_{bind} = k_{bind}/k_{unbind}$, $K_{in} = D_{out}/D_{in} \geq 1$, $\Gamma(\widehat{C}_I) = (b^2(\omega - \beta\delta)^2 + 2b\widehat{C}_I(\beta\delta + \omega) + \widehat{C}_I^2)^{1/2}$, $\omega = (\beta\phi + 1)K_{on}$, $\phi = (C_P/\rho) - (1 - \delta)/K_{on}$, and L_{in}^* is defined by Eq. S8. These expressions thus determine analytically how different parameters of the model affect the nontrivial steady state and the threshold (the transcritical bifurcation).

As discussed in the previous section, increasing the number of integrins inside the NA causes an increase in their area. According to the model, this may be accomplished directly through two approaches: 1) increasing the total number of integrins on the membrane through the parameter C_I or 2) increasing the likelihood that an integrin is inside the adhesion through the ligand concentration [Ligand] (see how K_{bind} is defined in M3b) or the reduction in diffusivity K_{in}. In the limit $C_I \to \infty$, the first approach yields adhesions with a finite size $A^\infty < h^2$ (see Eq. S10; Fig. 3 *A*). On the other hand, the limiting case for the second approach is equivalent to all integrins being inside the adhesion, where (according to Eq. 2) the area of the clustered steady state is given by

$$\overline{A}^* = A^*(C_I h^2) = \frac{h^2\left(\overline{\Gamma}\left(\overline{C}_I\right) - \overline{C}_I + b(\phi K_{on} - \delta)\right)}{2bK_{on}},$$

with $\overline{C}_I = K_{on}C_I$ and

$$\overline{\Gamma}\left(\overline{C}_I\right) = \left(b^2(\delta - \phi K_{on})^2 + 2b\overline{C}_I(\delta + \phi K_{on}) + \overline{C}_I^2\right)^{1/2}.$$

We note that $\overline{A}^* \leq A^\infty$ (see Fig. 3 *C*) and $\lim_{C_I \to \infty}\overline{A}^* = A^\infty$, which implies that ligand-dependent regulation of adhesion area cannot overcome integrin-dependent regulation. Furthermore, a stable adhesion plaque may also grow if more plaque material is introduced into the system. Within the model, this is controlled by the parameter C_P, which is linearly proportional to A^∞. Therefore, increasing C_P leads to unbounded growth of the adhesion area (see Fig. 3 *B*). Thus, the maximal area of NAs is regulated intracellularly through the parameters C_I and C_P, whereas the formation of adhesions and modulation of their area may be regulated intracellularly through these same parameters or extracellularly through [Ligand]. This, as a result, establishes a hierarchy in the determination of NA area by these three physiologically regulated densities, ranked according to their relative importance as follows: $C_P > C_I >$ [Ligand].

Effects of the magnitude and degree of coaggregation

To further understand the dynamics of the model, we will analyze the model under appropriate limits. Thus, we first

consider the integrin-independent adhesion-plaque formation when $\delta \to 0$. In this case, the model reduces to a fully deterministic version of the "bulk-on/bulk-off" adsorption model (30) with one added component for the conservation of matter. In this limit, we have $A^* \to A_0$, which implies that adhesion area should grow linearly with adaptor concentration (see Fig. 3 *B*). This demonstrates the basic chemical kinetic control system of the model. Regardless of integrin density, adhesion plaques may form if a large enough pool of adaptor proteins is present (i.e., $A_0 > 0$). In the absence of coaggregation, the cell must control both the formation and area of adhesions through the concentration of adaptor proteins. Interestingly, reductions in adaptor protein concentration have been found to decrease adhesion size (68–72). On the other hand, if there is coaggregation between integrins and adaptor proteins, the cell can set the maximal area of adhesions, A^∞, by varying adaptor protein concentration while controlling their formation with the density of integrins. This is in line with the recent findings that NA size saturates as integrin density (or activation) is increased (see Fig. 2; (18)), suggesting that the coaggregation of the two proteins is a critical component of the model needed to capture experimental observations.

By tracking the location of the threshold (the transcritical bifurcation in Fig. 3) as the values of both C_I and C_P are varied in a two-parameter bifurcation, we obtain two regimes of behavior separated by a monotonically decreasing boundary at a given value of δ (see Fig. 4 *A*). This boundary divides the first quadrant into the two regimes of unclustered (below) and clustered (above) steady states, with the former expanding at the expense of the latter as the magnitude of coaggregation δ is decreased. These results suggest that the adaptor protein concentration needed to induce clustering is always lower in the presence of coaggregation (see Fig. 4 *A*). The amount of reduction in adaptor protein density generated by the inclusion of coaggregation is given by

$$\begin{aligned} \Delta C_P^{\ddagger} &:= C_P^{\ddagger}\big|_{\delta=0} - C_P^{\ddagger}\big|_{\delta}, \\ &= \frac{\delta\rho}{K_{on}} \frac{(1+K_{bind})K_{in}C_I}{(b+(1+K_{bind})K_{in}C_I)} > 0. \end{aligned}$$

Interestingly, in the limit of infinite integrin density, we have

$$\lim_{C_I \to 0} C_P^{\ddagger} = \frac{\rho(1-\delta)}{K_{on}}$$

This suggests that even when integrin density is arbitrarily high, the cell can still turn off clustering by reducing C_P (or δ) to make ϕ negative.

To study the effects of altering the degree of cooperativity n on the steady-state dynamics of adhesion area, we plot in Fig. 4 *B* the stable branch of clustered steady states (i.e., the stable branch to the *right* of the threshold in Fig. 3 *A*) at various values of n. Our results reveal that increasing n increases the slope of A^* with respect to C_I and that in the limit as $n \to \infty$, we obtain a step-like switching response in which protein clusters form beyond a threshold in integrin density occurring right at the transcritical bifurcation point (see Fig. 4 *B*). The area of adhesions formed in this case remain roughly the same regardless of integrin density. Finally, we have used the maximal a posteriori estimate of $A(N_{in})$ (see Fig. 2) as means of estimating n numerically. This is done by solving for the nonzero A-nullcline with $n = 2, 3, 4$, where visual comparison with the data for $A(N_{in})$ suggests $n = 2$–3 (data not shown).

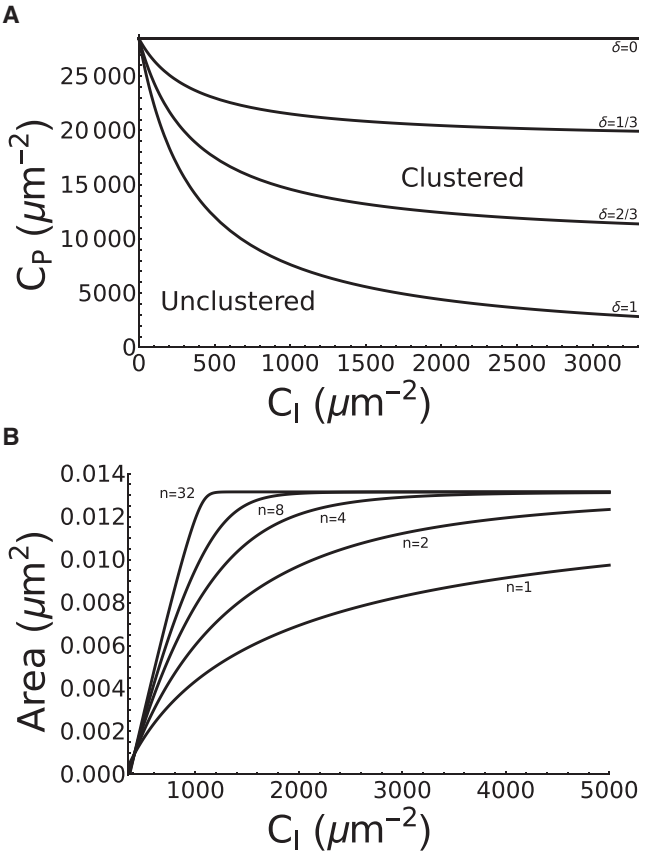

FIGURE 4 The effects of coaggregation and cooperativity on steady-state dynamics of protein clustering. (*A*) Two-parameter bifurcation of adhesion area A with respect to C_I and C_P are given, showing the boundary between the regimes of unclustered (*below*) and clustered (*above*) steady states for various values of coaggregation δ. The boundary is defined by the transcritical bifurcation points in Fig. 3 when C_I and C_P are both varied. Increasing δ reduces the adaptor protein density needed to induce aggregation. In the limit $\delta \to 0$, integrin density C_I has no effect on the aggregation of adaptor proteins. (*B*) Stable branches of the clustered steady states shown in Fig. 3 *A* for various degrees of cooperativity n are given. By increasing n, the density thresholds for clustering decreases, and the steepness of the stable branch of clustered steady states increases.

The effects of reduced integrin lateral mobility

The model assumes that integrin mobility is significantly reduced inside the NA (see O3 and O4) and that, at

equilibrium, this area is in turn dependent on the number of integrins it contains. This makes understanding the dependence of NA dynamics on changes in integrin lateral mobility nontrivial. We can quantitatively understand this by first noting that the area specified by Eq. 2 is a monotonically increasing function of the number of integrins inside the NA, N_{in}^*. Therefore, we may simply study the effects of the two parameters, which control changes in integrin lateral mobility (namely, K_{in} and K_{bind}), on the variable N_{in}^*. From Eq. 4 and Eq. S8, we have

$$N_{in}^* = (1+K_{bind})M_{in}^* = \frac{h^2\left((2\beta\phi+1)\widehat{C}_I - \Gamma\left(\widehat{C}_I\right) + b(\omega-\beta\delta)\right)}{2\beta\omega}.$$

We can thus conclude that N_{in}^* depends on integrin mobility only through the term $K_{in}(1+K_{bind})$ that appears implicitly in $\hat{C}_I$, ω, and β. This means that we cannot distinguish between the effects induced by the two parameters purely based on adhesion area or integrin content. On the other hand, the fraction of bound integrins, given by

$$\frac{L_{in}^*}{L_{in}^*+M_{in}^*} = \frac{K_{bind}}{1+K_{bind}},$$

depends explicitly on the binding affinity. This means that although both reduced diffusivity (K_{in}) and ligand binding (K_{bind}) will result in an increase in the area and integrin content of adhesions, only ligand binding can increase the fraction of bound integrins.

Because of the similarity of the effects of ligand binding and reduced diffusivity, we focus our attention on analyzing more closely the effects of ligand binding, noting that the same analysis can be performed to study the effects of reduced diffusivity. In the absence of binding, we obtain the following unbound steady state

$$\tilde{\mathbf{S}}^* = \lim_{K_{bind}\to 0}\left(A^*, M_{in}^*, L_{in}^*\right) = \left(\tilde{A}^*, \tilde{M}_{in}^*, 0\right),$$

which has the associated critical protein thresholds

$$\tilde{C}_I^\ddagger = \lim_{K_{bind}\to 0} C_I^\ddagger, \quad \text{and} \quad \tilde{C}_P^\ddagger = \lim_{K_{bind}\to 0} C_P^\ddagger. \tag{5}$$

Based on Eq. S11, we can conclude that $\tilde{C}_I^\ddagger$ is larger than $C_I^\ddagger$ by a factor of $1+K_{bind}$. Similarly, from Eq. S12, it can be shown that $\tilde{C}_P^\ddagger \geq C_P^\ddagger$. Thus another effect of binding (and reduced diffusivity) is that it increases the potency of integrins and adaptor proteins in the formation of adhesions by decreasing the threshold for clustering (i.e., shifting the transcritical bifurcation to the left) and expanding the range of stability of the clustered steady state (see Fig. 5 *A*).

For the more general scenario when $K_{bind} > 0$, we note that the state $\tilde{\mathbf{S}}^*$ is a biophysically relevant metastable steady

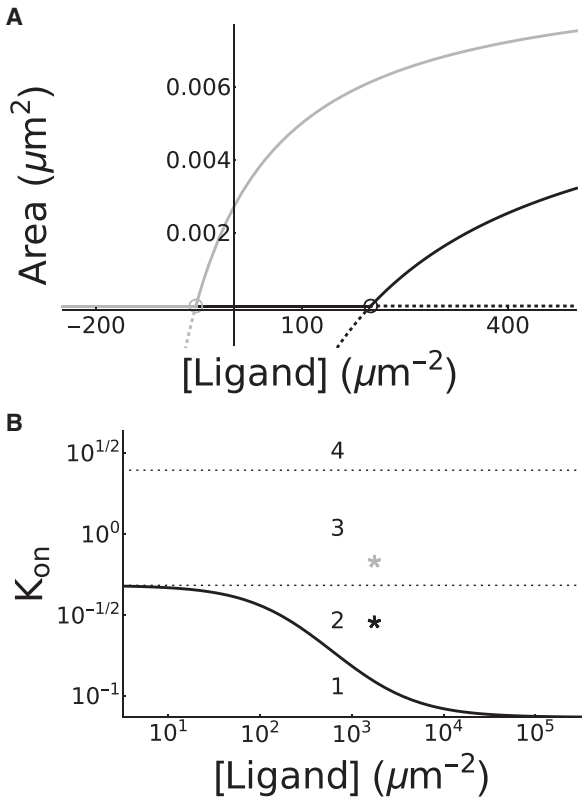

FIGURE 5 Distinct regions in parameter space are distinguished by their dependence on ligand binding. (*A*) A bifurcation diagram of adhesion area *A* with respect to [Ligand] is given, showing branches of stable (*solid lines*) and unstable (*dashed lines*) steady states separated by thresholds of transcritical bifurcation points (*open circles*). Decreasing K_{on} from 0.7 (*black lines*) to 0.3 (*gray lines*) shifts the transcritical bifurcation point to the left, allowing for the unclustered stable steady state to be attained at [Ligand] = 0. (*B*) Two-parameter bifurcation of adhesion area *A* with respect to [Ligand] and K_{on} is given, showing the boundary (*black line*) between the regions of unclustered (*region 1*) and clustered steady states lying below and above the boundary, respectively. The region of clustered steady states is further divided into three regions: region 2, defined by $[\text{Ligand}]^\ddagger > 0$, requiring the presence of both ligand and integrin to induce clustering; region 3, defined by $[\text{Ligand}]^\ddagger < 0$ with $A_0 < 0$, requiring the presence of integrin, but not necessarily ligand, to form stable adhesion plaques; and the unphysiological region 4, defined by $A_0 > 0$, which exhibits clustering irrespective of integrin or ligand densities.

state only if all its coordinates are non-negative. This is equivalent to the experimentally verifiable criterion $[\text{Ligand}]^\ddagger > 0$, which can be used to further divide parameter space into ligand-dependent and independent clustering regions (see Fig. 5). These regions are differentiated by their behavior in the limit as $[\text{Ligand}] \to 0^+$, where in the former region the stable unclustered steady state is attained (*black lines* in Fig. 5 *A*, with $K_{on} = 0.7$), whereas in the latter, the stable clustered steady state is attained (*gray lines* in Fig. 5 *A*, with $K_{on} = 0.3$). This implies that if the interactions between adaptor proteins are strong enough (e.g., if K_{on} is large enough; see Fig. 5 *B*), then adhesion plaques will form even in the absence of ligand binding. As discussed

in the previous section, it is even possible for these interactions to be strong enough to induce the formation of an adhesion plaque in complete absence of integrins (as suggested by *region 4*, where $A_0 > 0$). Together, these considerations allow us to identify four regions in parameter space:

1) *No Clustering (region 1 in* Fig. 5 B*):* This occurs when [Ligand] $<$ [Ligand]‡, and the model predicts there is no clustering of adaptor proteins.
2) *Ligand-Dependent Clustering (region 2 in* Fig. 5 B*):* This region is bounded by [Ligand]$^{\ddagger} \leq$ [Ligand] with [Ligand]$^{\ddagger} > 0$. Within this region, the model predicts clustering occurs only when [Ligand] is high enough.
3) *Ligand-Independent Clustering (region 3 in* Fig. 5 B*):* This region is defined by [Ligand]$^{\ddagger} \leq$ [Ligand] with [Ligand]$^{\ddagger} < 0$ and $A_0 < 0$. Within this region, the model predicts clustering to occur regardless of the value of [Ligand].
4) *Integrin-Independent Clustering (region 4 in* Fig. 5 B*):* This region is defined by $A_0 > 0$. Within this region, the model predicts clustering regardless of the value of [Ligand] and C_I. This appears to be unphysiological.

Because clustering is absent in region 1 and unphysiological in region 4, one may conclude that cells have likely tuned the interaction of adaptor proteins and integrins to that in regions 2 or 3, which differ by whether or not adhesions form in the absence of ligand. Whereas some have hypothesized that activation of integrins by adaptor proteins may be sufficient to induce clustering of integrins (73), an observation consistent with the model in region 3, others have shown that a ligand spacing greater than ~60 nm drastically reduces the spreading of cells (74–76), an observation more consistent with crossing the transcritical bifurcation point in region 2. These two mutually exclusive hypotheses are considered to determine the two distinct sets of parameter values used to generate the curves in Fig. 5 *A* (see Parameter Estimation).

Mechanosensitive ligand binding dynamics

Thus far, we have not explicitly considered the effects of force on NA formation, although it is known that adhesions transmit force to the ECM. Mechanical forces can accelerate the dissociation of the integrin-ligand bond (see O5 and M3c in Methods). Moreover, a collection of catch bonds under fixed load will catastrophically fail once the number of bound integrins drops below a threshold (47). Therefore, to effectively transmit force to its environment, an NA must contain a sufficient number of bound integrins. This raises the question of how the dynamics of force generation in NAs are manifested or, more specifically, whether adhesion load (the total force) or stress (force per unit area) is the fixed mechanical parameter that allows for NA assembly from a single integrin-adaptor protein complex (32,36,77).

If adhesion load is held constant, then adhesions needs to build up a sufficient integrin content to be able to bear the load. As shown earlier, a large equilibrium integrin content at steady state can be achieved by either increasing K_{in} or K_{bind}. However, previous work has found that clusters of catch bonds will disassemble when there are a small number of bound integrins (47). Therefore, it is unclear how adhesions reach their stable equilibrium under fixed load. Alternatively, if stress is held constant, then the fraction of bound integrins must be large enough to bear the variable load that increases as the adhesion grows. The latter requires that K_{bind} be large enough (as discussed before). The mechanosensitivity of the integrin-ligand bond and the complex spatial dynamics of integrins make resolving this question nontrivial.

Bistable switch in regions 2 and 3 with respect to stress

To explore the effect of mechanical force on dynamics, we expand our equilibrium mean-field model described by Eqs. 1a, 1b, and 1c to include the mechanosensitive binding affinity of integrin, as described by Eqs. S16 and S17 (for further details, see Supporting Materials and Methods). Our initial analysis, as well as previous studies (28,29,47), suggest that there is a maximal stress, σ_c, that NAs can sustain. To further expand on this result, we plot in Fig. 6 the dependence of the steady-state adhesion area A^* (and $\tilde{A}^*$ in region 3) with respect to stress σ and label the different branches of the curve based on the stability properties of the steady states belonging to each branch (using the subscripts "s" and "u" to label the stable and unstable ones, respectively). The resulting bifurcation diagram shows that the dynamics are governed by a bistable switch possessing a hysteresis, similar to those previously observed in systems of the Rho family of GTPases (8,59). The switch has a plateaued branch of elevated steady states (*black line*), labeled A_s^*, merging with another branch of unstable saddle points beneath it (*dashed black line*), labeled A_u^*, at a saddle-node bifurcation when $\sigma_c \approx 470$ kPa. In region 3, bistability is produced by another lower branch of metastable states formed by $\tilde{A}^*$ (*gray line* in Fig. 6 *B*), whereas the branch $A = 0$ is unstable. In region 2, the unstable branch A_u^* intersects $A = 0$ at some value of stress σ_t ($0 \leq \sigma_t \leq \sigma_c$), leading to the formation of a transcritical bifurcation that produces a region of monostability for $\sigma < \sigma_t$ (*horizontal dashed line* in Fig. 6 *A*) and bistability for $\sigma > \sigma_t$ (*horizontal solid line* in Fig. 6 *A*).

The folded elevated stable and unstable branches seen in Fig. 6 have been previously reported in studies that considered only the number of liganded bonds (28,29,47) or adaptor proteins in the adhesion (41); these studies have reported either a monotonically decreasing elevated stable branch (28,29) or one that increases significantly with applied force or ECM stiffness (41,47). In either case, a lower stable/metastable branch ($\mathbf{Z} = (0, 0, 0)$ in region 2 with $\sigma > \sigma_t$ and the previously defined $\tilde{\mathbf{S}}^* = (\tilde{A}^*, \tilde{M}_{in}^*, 0)$ in region 3 with $\sigma < \sigma_c$) has not been previously reported for a model that considered only liganded bonds. Our results thus show that the system possesses bistability between clustered and the unbound or unclustered steady states,

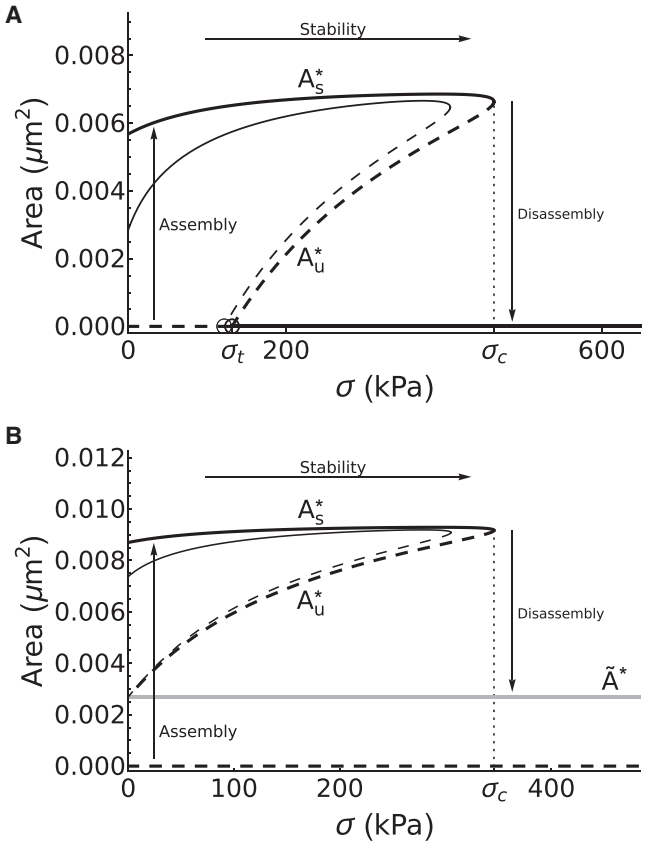

FIGURE 6 The effects of integrin mechanosensitivity on NA area and integrin content. Bifurcation diagram of adhesion area with respect to stress as determined by (*A*) region 2, and (*B*) region 3, showing a bistable switch with two semiplateaued stable branches of steady states (*solid lines*), one of which is elevated, representing A_s^* (*black*), whereas the other is lower, representing $\tilde{A}^*$ (*gray*), separated by an unstable branch of saddle points A_u^* (*short-dashed black line*). A_s^* and A_u^* merge at a threshold determined by a saddle-node bifurcation point at $\sigma = \sigma_c$. Beyond this critical stress σ_c, all integrins rapidly unbind and adhesions disassemble to (*A*) the unclustered steady state or (*B*) the unbound steady state $\tilde{A}^*$. In region 2 (*A*), the unstable branch undergoes a transcritical bifurcation at $\sigma = \sigma_t$ (*open circles*), producing a region of monostability where adhesions may directly assemble to the stable branch. Thick lines: [Ligand] = 8050 μm^{-2}; thin lines: [Ligand] = 2012.5 μm^{-2}.

indicating that this bistability arises from the consideration of plaque dynamics. We denote the elevated stable and middle unstable branches by $\mathbf{S}^* = (A_s^*, M_s^*, L_s^*)$ and $\mathbf{U}^* = (A_u^*, M_u^*, L_u^*)$, respectively. These two steady states correspond to large clusters of integrins bearing a small load and small clusters bearing large loads, respectively. This correspondence may also be used to intuitively understand their stability because the small (unstable) clusters will unbind catastrophically once a single integrin-ligand bond ruptures, whereas the large (stable) clusters contain enough integrins for rebinding effects to outpace unbinding.

NA dynamics as determined by the bistable switch

Near the saddle node of Fig. 6, *A* and *B* (i.e., near $\sigma \approx \sigma_c$), the basin of attraction of the clustered steady states shrinks significantly until it eventually disappears, along with the steady state, when $\sigma > \sigma_c$. This means that the number of bound integrins at the steady state $\mathbf{S}^*$ are incapable of supporting the imposed stress, causing integrins within the NA to catastrophically unbind and the NA area to revert to the unbound steady state $\tilde{A}^*$ in region 3 (Fig. 6 *A*) and to $A = 0$ in region 2 (Fig. 6 *A*). This type of behavior corresponds to NA disassembly. On the other hand, in region 3 with $\sigma < \sigma_c$, stochastic fluctuations in the number of integrins inside the adhesion plaque can cause the system to jump from the unbound steady states $\tilde{A}^*$ to the clustered steady states A_s^*. In contrast to the previous jump, this type of behavior corresponds to NA assembly. Alternatively, in the monostable regime of region 2 (see *dashed horizontal line* in Fig. 6 *A*), there is no barrier to cross for assembly, and NAs may form in a noise-independent manner. Interestingly, in both regions, the model predicts that the stable NA area A_s^* does not vary significantly for a whole range of stress between $[0, \sigma_c]$ because of the plateau nature of the upper stable branch. This suggests that NAs may go through a cycle of adhesion assembly, stability, and disassembly based on the magnitude of stress exerted on them, as previously seen experimentally (18,50).

We have also investigated the effects of reduced ligand concentration on the mechanosensitivity of adhesions by reducing the value of [Ligand] fourfold (see *thin lines* in Fig. 6). Here, we observe two notable differences in the model outcomes. Firstly, when ligand concentration is reduced, the area of NAs under zero force (e.g., $\sigma = 0$) is reduced, whereas the maximal value it attains remains roughly the same. This suggests that NAs, in these conditions, can exhibit significant reinforcement because of force, increasing in size upon application of force. This reinforcement is similar to what has been previously observed experimentally (78) and in other theoretical models of focal adhesions (36,48), as well as clusters of catch bonds (47). Secondly, we also find that the critical stress σ_c decreases when ligand concentration is reduced. This implies that the primary effect of reducing ligand concentration on NAs is to make them more susceptible to forces by 1) making their area more force-dependent and 2) making them more likely to catastrophically disassemble because of force.

Stochastic simulation of the model

It has been previously shown through stochastic simulations that the upper branches of Fig. 6 are metastable equilibria for clusters of catch bonds with a fixed load and that upon crossing the lower branch, the cluster undergoes disassembly in which all bonds rapidly unbind (47).

By running stochastic simulations with $\sigma \approx \sigma_c$ (see Supporting Materials and Methods for more details on the implementation), the model also produces NA disassembly under fixed stress regardless of the region (see Fig. 7 *A* for

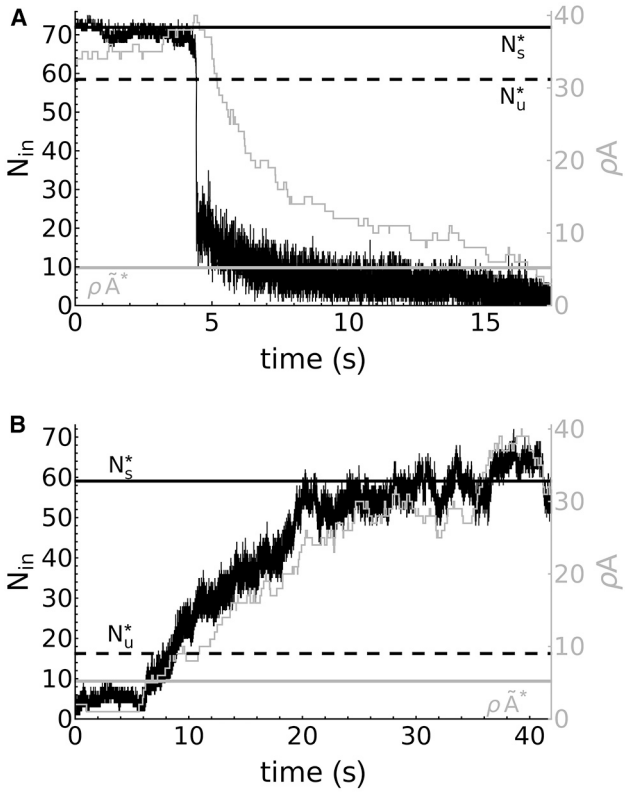

FIGURE 7 The assembly and disassembly of NAs is a force-dependent process. (*A* and *B*) Stochastic simulations of the number of bound integrins (*thin black lines*) and adaptor proteins (*thin gray lines*) during assembly and disassembly are shown. (*A*) Under high stress ($\sigma = 0.92\sigma_c$) and starting from the equilibrium **S*** (*thick black horizontal line*), integrins within NAs undergo catastrophic unbinding upon crossing the stable manifold of the saddle **U*** (*dotted black horizontal line*), leading to disassembly as they diffuse away from the adhesion area. (*B*) A long-lived NA state is formed, starting from a single integrin-adaptor protein complex, when the applied stress is low ($\sigma = 0.25\sigma_c$). This process is driven primarily by plaque growth toward the metastable state with $A = \tilde{A}^*$ (*thick gray horizontal line*), which, in conjunction with ligand binding, increases N_{in}, the number of integrins inside the NA, until it crosses the stable manifold of the saddle point **U***. Beyond the stable manifold of **U***, the trajectory flows to the stable steady state **S***. Black horizontal lines are identical to those in (*A*).

simulations associated with *region 3*) and for fixed load (data not shown). The stochastic simulation of the model also exhibits NA assembly from a single integrin-adaptor protein complex (see Fig. 7 *A*). In region 2 with $\sigma < \sigma_t$, NA assembly reaches **S*** unimpeded by **U*** because of the lack of bistability for $0 \leq \sigma < \sigma_t$, whereas in region 3 (see Figs. 6 *B* and 7 *B*), the system must cross the stable manifold of **U***. This manifold forms a threshold (highlighted by the *dashed line* in Fig. 7) that determines whether the system jumps from 1) the single integrin-adaptor complex to the clustered steady state **S*** (*black solid line* in Fig. 7 *B*) during assembly, passing through the unbound metastable state $\tilde{\mathbf{S}}^*$ (gray line), or from 2) the clustered steady **S*** (*black solid line* in Fig. 7 *B*) to the unbound metastable state $\tilde{\mathbf{S}}^*$ (*gray line*) during disassembly. The mechanical conditions that allow for a stochastic jump to cross the barrier created by the unstable state were not previously determined (41,47). In this study, we have explored 1) under what conditions noise-driven NA assembly occurs and 2) what role bistability plays in this process.

To verify whether the model under fixed adhesion load produces results consistent with those previously seen (28,29,34,47), we also performed stochastic simulations starting from a single integrin-adaptor protein complex, in which adhesion load is held fixed. In this scenario, assembly is only observed for very small fixed loads (less than ~1% of the critical load), as the force per integrin of small adhesions with a fixed load overwhelmingly favors the unbinding of integrin (data not shown). This is in agreement with the previous finding that fixed loads can only lead to adhesion disassembly (41,47). Interestingly, with the model presented here, we do observe assembly for fixed stresses arbitrarily close to the critical stress σ_c, albeit exceedingly rarely. This highlights the unique nature of the model, which identifies fixed stress as a mechanical condition allowing for NA assembly and predicts that cells can occasionally assemble NAs even at very high stresses.

The bistability characterizing this model also plays an important role in reaching the elevated steady state **S***. Near the initial condition of a single integrin-adaptor protein complex, diffusion stochastically adds and removes integrins from underneath the adhesion plaque. However, as can be seen in Fig. 7 *A*, these stochastic fluctuations do not bring the system close enough to the saddle point **U*** (*dotted line*) to cross its stable manifold. The metastable state $\tilde{\mathbf{S}}^*$, on the other hand, acts as an attractor for the system, initiating the first phase of a robust growth in the adhesion plaque. In conjunction with ligand binding, this eventually pushes the system past the stable manifold of the saddle **U***, allowing it to reliably reach the elevated stable steady state **S***. As highlighted before, because fixed stress (but not fixed load) is permissive to ligand binding during the growth phase, we may conclude that the mechanical constraint on the system and the bistability with the metastable attractor $\tilde{\mathbf{S}}^*$ allows for the system to overcome the kinetic barrier created by the unstable steady state **U*** such that adhesions may form from a single integrin-adaptor protein complex.

DISCUSSION

In this study, we presented a biophysical model of NA formation as a condensed phase of adaptor proteins and integrins that forms along at the interface of the cytoplasm and the cell membrane because of a mechanism we term coaggregation. From this biophysical model, we constructed a three-dimensional minimal mathematical model of adhesion dynamics near equilibrium and a computational framework for realizing discrete simulations of adhesion formation. The nonlinearities included in the mathematical model

were adapted from the biophysical framework used to describe NAs. The near-equilibrium dynamics used to analyze the stability of the equilibria showed that adhesions form with an area and integrin content specified by $\mathbf{S}^*$ once integrins, adaptor proteins, or extracellular ligands cross a well-defined density threshold. These thresholds are defined by transcritical bifurcation points at which a stable branch of clustered steady states emerges in each case. We analytically determined the dependence of these thresholds on model parameters as specified by Eqs. S11–S13. Our analysis of these results revealed that the stable branch plateaus at high integrin or ligand density but monotonically increases with respect to adaptor protein density, suggesting that adaptor proteins play a key role in regulating the size of NAs. It also showed that there is a hierarchy in the relative importance of the three protein densities regulating NA area, given by adaptor proteins > integrins > extracellular ligands. The dependence of $\mathbf{S}^*$ on biophysical parameters was then analyzed to demonstrate that the immobilization of integrins upon binding to ligands inside the adhesion area (controlled by K_{bind}) lowers the density thresholds for adhesion formation.

In contrast to previous models of adhesions (32–34,36), we did not assume that the average density of integrins inside the adhesion plaque is a fixed quantity. This assumption is necessary for the model to be consistent with the observation that the integrin density measured in adhesions varies significantly within the same cell (79) and is motivated by the nonlinear relation between NA area and its integrin content (see Fig. 2). Our model accounted for the variable density of integrins by considering their interactions with adaptor proteins forming the adhesion plaque, which spatially delimits the adhesion area. Similar interactions have also been considered in a more biophysically detailed model of adhesion dynamics (38), but the simplicity of the model presented here compared to this previous study allowed for further theoretical analysis of this system. Interestingly, it was previously estimated that the upper limit of N_{in}/A is ~25,000 μm^{-2} using structural considerations (18), but the results of our conditional expectation analysis suggest that the effective limit of integrin density in the adhesion may be as low as ~17,000 μm^{-2}. Below this threshold, NA area may be a result of the tethering mechanism described by Eq. S7, whereas above this threshold, adhesion area was the result of integrin crowding, which may be indicative of NAs transitioning to more mature classes of adhesions such as focal complexes. To the best of the authors' knowledge, the tethering mechanism proposed here represents a novel understanding of adhesion stabilization by integrins.

Because of the apparent isotropic growth of NAs (50), we have not considered anisotropic effects of compression and/or stretching on adaptor protein adsorption as has been done in other models (3,32). This can be justified by the fact that the dynamic nature of adaptor-cytoskeletal interactions leads to slippage under force (80), producing a viscoelastic mechanical response, in which the effects of elasticity is lost on long timescales (e.g., at equilibrium). Furthermore, it was previously argued that the interactions between adaptor proteins are unlikely to be strong enough for the energy of deformation of the adhesion plaque to have a significant effect on the outcome of the adhesion formation process (36). This assumption allowed us to use a simpler model of adaptor protein adsorption (30) and incorporate the effects of force in a manner that can be directly linked to experimental single-molecule observations (42).

The mechanosensitive properties of integrin unbinding were included in the model as a force-dependent bond lifetime (see Eq. S14). Using this to determine integrin binding affinity, we managed to compute the equilibrium area of the adhesion as a function of applied force, revealing a saddle-node bifurcation at a critical value of stress (see Fig. 6 *D*). Beyond this value of stress, all the integrins in the adhesion rapidly become unbound from their ligands, and tension is no longer transmitted to the extracellular environment. Similar phenomena had been previously observed in other studies for fixed values of adhesion load (28,29,47). By considering the effects of integrin content on the area of the adhesion plaque, we were able to use adhesion stress rather than load as a bifurcation parameter and study how its steady-state effects may give rise to a mechanically regulated NA lifecycle. We demonstrated that such a lifecycle is governed by a bistable switch with a saddle-node bifurcation when NA area is plotted against fixed stress. The saddle node acts as a threshold for adhesion disassembly, the last phase of the lifecycle. Increasing the ligand concentration made the upper branch of the bistable switch more plateaued such that increasing or decreasing the stress within a given range has little to no effect on NA area.

Consistent with previous studies, stochastic realizations of our model with high values of stress (or load; data not shown) produced NA disassembly close to the threshold determined by the saddle-node bifurcation, causing the trajectory to jump from the upper to the lower stable branch of the bistable switch. The jump is due either to crossing the threshold or to stochastic effects pushing trajectories beyond the stable manifold of the saddle points in the middle branch, leading to the rapid unbinding of all integrins in the adhesion, followed by slow adhesion-plaque disassembly.

The process of adhesion-plaque assembly, initiated from a single integrin-adaptor complex, was found to have a more diverse set of dynamics than disassembly. First, we discovered that unlike during disassembly, the accumulation of bound integrins inside the adhesion area and the growth of the adhesion plaque occur on a similar timescale during assembly. Second, we identified a region in parameter space (*region 2* in Figs. 5 *B* and 6 *A* with $\sigma < \sigma_t$) where assembly occurs independently of stochastic effects. This finding is noteworthy because previous models had reported, in their

mean-field analysis, the presence of an unstable steady state that blocks the assembly of very small adhesions (41,47). The mean-field analyses were performed using a one-variable setting in which the only way to reach the state corresponding to stable adhesions was through stochastic jump effects that were not very well understood. The mean-field analysis performed here was done in a three-variable setting in which it was possible to shift the position of the unstable state to a nonphysical regime, thus minimizing its interference with the flow of trajectories toward the upper stable steady state.

The difference in outcomes between this study and previous ones can also be attributed to the mechanical condition we considered in this study (fixed stress). This may be understood intuitively by the fact that, when stress is fixed, a small adhesion will have a correspondingly small load. However, when load is fixed (28,29,34,47), the integrin bonds break too quickly for the equilibrium with area A^* to be readily attained. In previous models of clustered bonds, there was no explicit adhesion area, and therefore, adhesion stress could not be defined in these models (28,29,34,47). In this study, we resolved this by considering the adsorption dynamics of the adaptor proteins that form the adhesion plaque (30). Experimentally, NA formation and area were found to be independent of traction force, whereas they disassemble in a force-dependent manner (18). These findings are consistent with our model predictions under fixed stress (but not fixed load), showing that NAs assemble to a roughly constant area for a wide range of stresses and disassemble at high stresses.

Similar to previous studies, the model also showed that there is a regime in parameter space within which the stable manifold of the saddle points acts as a barrier that can be crossed with stochastic effects (see *region 3* in Figs. 5 *B* and 6 *B*). Within this regime, we demonstrated that fixing adhesion stress (but not load) allows for the assembly of adhesions and that bistability between the elevated steady state $\mathbf{S}^*$ and the metastable state $\tilde{\mathbf{S}}^*$ plays a significant role in determining the dynamics of assembly in this region of parameter space. When we fixed the value of load (rather than stress), we found that assembly is exceedingly rare for nonzero values of load ($>1\%$ the critical load; data not shown).

As suggested above, the mechanical control of the NA lifecycle, including assembly, stability, and disassembly, may be explained by a bistable switch (possessing a hysteresis) with respect to adhesion stress and that this stress, rather than the total adhesion load, is the mechanical parameter conserved during noise-driven NA assembly. As stress increases, NA area may increase (causing adhesion reinforcement) when extracellular ligand density is low or remain relatively constant when it is high. Once stress becomes large enough, NA disassembly can be initiated either by stochastic effects driving the system beyond a threshold corresponding to the stable manifold of saddle points in the middle branch of the bistable switch or by an excess buildup of force pushing the system beyond the saddle node of this switch.

Increasing the complexity of the model presented here by considering different types of adaptor proteins forming the adhesion plaque to examine their effects on dynamics represents an interesting direction to pursue. This could be also combined with studying the effect of actin branching and bundling on NA dynamics. The latter, although very technically challenging, can provide further insights onto how they may exert force on the adhesion plaque.

SUPPORTING MATERIAL

Supporting Material can be found online at https://doi.org/10.1016/j.bpj.2019.08.004.

AUTHOR CONTRIBUTIONS

L.M. conceived the biophysical model, analyzed it, wrote the code for simulations, and drafted the manuscript. A.K. substantially revised the manuscript and provided supervision throughout the project.

ACKNOWLEDGMENTS

Discussion with Prof. Claire Brown, Department of Physiology, McGill University, greatly benefited the development of this work.

This work was supported by the Fonds Nature et technologies, Gouvernement du Quebec (http://www.frqnt.gouv.qc.ca/en/accueil) team grant to A.K. L.M. was supported by the NSERC-CREATE in Complex Dynamics Graduate Scholarship.

SUPPORTING CITATIONS

References (81–103) appear in the Supporting Material.

REFERENCES

1. Friedl, P., and D. Gilmour. 2009. Collective cell migration in morphogenesis, regeneration and cancer. *Nat. Rev. Mol. Cell Biol.* 10:445–457.

2. Luster, A. D., R. Alon, and U. H. von Andrian. 2005. Immune cell migration in inflammation: present and future therapeutic targets. *Nat. Immunol.* 6:1182–1190.

3. Li, L., Y. He, …, J. Jiang. 2013. Collective cell migration: implications for wound healing and cancer invasion. *Burns Trauma.* 1:21–26.

4. Clark, A. G., and D. M. Vignjevic. 2015. Modes of cancer cell invasion and the role of the microenvironment. *Curr. Opin. Cell Biol.* 36:13–22.

5. Lo, C. M., H. B. Wang, …, Y. L. Wang. 2000. Cell movement is guided by the rigidity of the substrate. *Biophys. J.* 79:144–152.

6. Devreotes, P., and C. Janetopoulos. 2003. Eukaryotic chemotaxis: distinctions between directional sensing and polarization. *J. Biol. Chem.* 278:20445–20448.

7. Mori, Y., A. Jilkine, and L. Edelstein-Keshet. 2008. Wave-pinning and cell polarity from a bistable reaction-diffusion system. *Biophys. J.* 94:3684–3697.

8. Lin, B., W. R. Holmes, …, A. Levchenko. 2012. Synthetic spatially graded Rac activation drives cell polarization and movement. *Proc. Natl. Acad. Sci. USA.* 109:E3668–E3677.
9. Thomas Parsons, J., A. R. Horwitz, and M. A. Schwartz. 2010. Cell adhesion: integrating cytoskeletal dynamics and cellular tension. *Nat. Rev. Mol. Cell Biol.* 11:633–643.
10. Chan, C. E., and D. J. Odde. 2008. Traction dynamics of filopodia on compliant substrates. *Science.* 322:1687–1691.
11. Morse, E. M., N. N. Brahme, and D. A. Calderwood. 2014. Integrin cytoplasmic tail interactions. *Biochemistry.* 53:810–820.
12. Liu, S., D. A. Calderwood, and M. H. Ginsberg. 2000. Integrin cytoplasmic domain-binding proteins. *J. Cell Sci.* 113:3563–3571.
13. Zaidel-Bar, R., S. Itzkovitz, …, B. Geiger. 2007. Functional atlas of the integrin adhesome. *Nat. Cell Biol.* 9:858–867.
14. Schiller, H. B., and R. Fässler. 2013. Mechanosensitivity and compositional dynamics of cell-matrix adhesions. *EMBO Rep.* 14:509–519.
15. Horton, E. R., A. Byron, …, M. J. Humphries. 2015. Definition of a consensus integrin adhesome and its dynamics during adhesion complex assembly and disassembly. *Nat. Cell Biol.* 17:1577–1587.
16. Schiller, H. B., M. R. Hermann, …, R. Fässler. 2013. β1- and αv-class integrins cooperate to regulate myosin II during rigidity sensing of fibronectin-based microenvironments. *Nat. Cell Biol.* 15:625–636.
17. Smith, M. A., L. M. Hoffman, and M. C. Beckerle. 2014. LIM proteins in actin cytoskeleton mechanoresponse. *Trends Cell Biol.* 24:575–583.
18. Changede, R., X. Xu, …, M. P. Sheetz. 2015. Nascent integrin adhesions form on all matrix rigidities after integrin activation. *Dev. Cell.* 35:614–621.
19. Changede, R., H. Cai, …, M. P. Sheetz. 2018. Ligand geometry controls adhesion formation via integrin clustering. *bioRxiv* https://doi.org/10.1101/435826.
20. Kucik, D. F., M. L. Dustin, …, E. J. Brown. 1996. Adhesion-activating phorbol ester increases the mobility of leukocyte integrin LFA-1 in cultured lymphocytes. *J. Clin. Invest.* 97:2139–2144.
21. Kucik, D. F. 2002. Rearrangement of integrins in avidity regulation by leukocytes. *Immunol. Res.* 26:199–206.
22. Nishida, N., C. Xie, …, T. A. Springer. 2006. Activation of leukocyte beta2 integrins by conversion from bent to extended conformations. *Immunity.* 25:583–594.
23. Luo, B. H., C. V. Carman, and T. A. Springer. 2007. Structural basis of integrin regulation and signaling. *Annu. Rev. Immunol.* 25:619–647.
24. Yu, T., X. Wu, …, D. F. Kucik. 2010. Affinity, lateral mobility, and clustering contribute independently to beta 2-integrin-mediated adhesion. *Am. J. Physiol. Cell Physiol.* 299:C399–C410.
25. Rossier, O., V. Octeau, …, G. Giannone. 2012. Integrins β1 and β3 exhibit distinct dynamic nanoscale organizations inside focal adhesions. *Nat. Cell Biol.* 14:1057–1067.
26. Welf, E. S., and J. M. Haugh. 2011. Signaling pathways that control cell migration: models and analysis. *Wiley Interdiscip. Rev. Syst. Biol. Med.* 3:231–240.
27. van Kooyk, Y., S. J. van Vliet, and C. G. Figdor. 1999. The actin cytoskeleton regulates LFA-1 ligand binding through avidity rather than affinity changes. *J. Biol. Chem.* 274:26869–26877.
28. Erdmann, T., and U. S. Schwarz. 2004. Stochastic dynamics of adhesion clusters under shared constant force and with rebinding. *J. Chem. Phys.* 121:8997–9017.
29. Schwarz, U. S., T. Erdmann, and I. B. Bischofs. 2006. Focal adhesions as mechanosensors: the two-spring model. *Biosystems.* 83:225–232.
30. Gov, N. S. 2006. Modeling the size distribution of focal adhesions. *Biophys. J.* 91:2844–2847.
31. Cirit, M., M. Krajcovic, …, J. M. Haugh. 2010. Stochastic model of integrin-mediated signaling and adhesion dynamics at the leading edges of migrating cells. *PLoS Comput. Biol.* 6:e1000688.
32. Nicolas, A., and S. A. Safran. 2006. Limitation of cell adhesion by the elasticity of the extracellular matrix. *Biophys. J.* 91:61–73.
33. Besser, A., and S. A. Safran. 2006. Force-induced adsorption and anisotropic growth of focal adhesions. *Biophys. J.* 90:3469–3484.
34. Sabass, B., and U. S. Schwarz. 2010. Modeling cytoskeletal flow over adhesion sites: competition between stochastic bond dynamics and intracellular relaxation. *J. Phys. Condens. Matter.* 22:194112.
35. Zhao, T., Y. Li, and A. R. Dinner. 2009. How focal adhesion size depends on integrin affinity. *Langmuir.* 25:1540–1546.
36. Olberding, J. E., M. D. Thouless, …, K. Garikipati. 2010. The non-equilibrium thermodynamics and kinetics of focal adhesion dynamics. *PLoS One.* 5:e12043.
37. Welf, E. S., U. P. Naik, and B. A. Ogunnaike. 2012. A spatial model for integrin clustering as a result of feedback between integrin activation and integrin binding. *Biophys. J.* 103:1379–1389.
38. Wu, Z., S. V. Plotnikov, …, J. Liu. 2017. Two distinct actin networks mediate traction oscillations to confer focal adhesion mechanosensing. *Biophys. J.* 112:780–794.
39. Cao, X., Y. Lin, …, V. B. Shenoy. 2015. A chemomechanical model of matrix and nuclear rigidity regulation of focal adhesion size. *Biophys. J.* 109:1807–1817.
40. Cao, X., E. Ban, …, V. B. Shenoy. 2017. Multiscale model predicts increasing focal adhesion size with decreasing stiffness in fibrous matrices. *Proc. Natl. Acad. Sci. USA.* 114:E4549–E4555.
41. Walcott, S., D. H. Kim, …, S. X. Sun. 2011. Nucleation and decay initiation are the stiffness-sensitive phases of focal adhesion maturation. *Biophys. J.* 101:2919–2928.
42. Kong, F., A. J. García, …, C. Zhu. 2009. Demonstration of catch bonds between an integrin and its ligand. *J. Cell Biol.* 185:1275–1284.
43. Bell, G. I. 1978. Models for the specific adhesion of cells to cells. *Science.* 200:618–627.
44. Pereverzev, Y. V., O. V. Prezhdo, and E. V. Sokurenko. 2009. Allosteric role of the large-scale domain opening in biological catch-binding. *Phys. Rev. E Stat. Nonlin. Soft Matter Phys.* 79:051913.
45. Li, Z., F. Kong, and C. Zhu. 2016. A model for cyclic mechanical reinforcement. *Sci. Rep.* 6:35954.
46. Li, J., and T. A. Springer. 2017. Integrin extension enables ultrasensitive regulation by cytoskeletal force. *Proc. Natl. Acad. Sci. USA.* 114:4685–4690.
47. Novikova, E. A., and C. Storm. 2013. Contractile fibers and catch-bond clusters: a biological force sensor? *Biophys. J.* 105:1336–1345.
48. Nicolas, A., B. Geiger, and S. A. Safran. 2004. Cell mechanosensitivity controls the anisotropy of focal adhesions. *Proc. Natl. Acad. Sci. USA.* 101:12520–12525.
49. Yu, C. H., J. B. Law, …, M. P. Sheetz. 2011. Early integrin binding to Arg-Gly-Asp peptide activates actin polymerization and contractile movement that stimulates outward translocation. *Proc. Natl. Acad. Sci. USA.* 108:20585–20590.
50. Choi, C. K., M. Vicente-Manzanares, …, A. R. Horwitz. 2008. Actin and alpha-actinin orchestrate the assembly and maturation of nascent adhesions in a myosin II motor-independent manner. *Nat. Cell Biol.* 10:1039–1050.
51. Wolfenson, H., A. Lubelski, …, B. Geiger. 2009. A role for the juxtamembrane cytoplasm in the molecular dynamics of focal adhesions. *PLoS One.* 4:e4304.
52. Digman, M. A., C. M. Brown, …, E. Gratton. 2008. Paxillin dynamics measured during adhesion assembly and disassembly by correlation spectroscopy. *Biophys. J.* 94:2819–2831.
53. Chi, L. C., J. S. Aguilar, …, M. A. Digman. 2014. Nanoimaging of focal adhesion dynamics in 3D. *PLoS One.* 9:e99896.
54. Le Dévédec, S. E., B. Geverts, …, B. van de Water. 2012. The residence time of focal adhesion kinase (FAK) and paxillin at focal adhesions in renal epithelial cells is determined by adhesion size, strength and life cycle status. *J. Cell Sci.* 125:4498–4506.
55. Tsunoyama, T. A., Y. Watanabe, …, A. Kusumi. 2018. Super-long single-molecule tracking reveals dynamic-anchorage-induced integrin function. *Nat. Chem. Biol.* 14:497–506.

56. Brown, C. M., B. Hebert, …, P. W. Wiseman. 2006. Probing the integrin-actin linkage using high-resolution protein velocity mapping. *J. Cell Sci.* 119:5204–5214.

57. Alexandrova, A. Y., K. Arnold, …, A. B. Verkhovsky. 2008. Comparative dynamics of retrograde actin flow and focal adhesions: formation of nascent adhesions triggers transition from fast to slow flow. *PLoS One.* 3:e3234.

58. Gupton, S. L., K. Eisenmann, …, C. M. Waterman-Storer. 2007. mDia2 regulates actin and focal adhesion dynamics and organization in the lamella for efficient epithelial cell migration. *J. Cell Sci.* 120:3475–3487.

59. Tang, K., C. G. Boudreau, …, A. Khadra. 2018. Paxillin phosphorylation at serine 273 and its effects on Rac, Rho and adhesion dynamics. *PLoS Comput. Biol.* 14:e1006303.

60. Doedel, E. J., T. F. Fairgrieve, …, X. Wang. 2007. AUT0–07p: continuation and bifurcation software for ordinary differential equations. Concordia University https://www.macs.hw.ac.uk/∼gabriel/auto07/auto.html.

61. MacKay, L., and A. Khadra. 2019. Data from: dynamics of mechanosensitive nascent adhesion formation. Anmar Khadra Repository 2019. Deposited July 30, 2019. http://www.medicine.mcgill.ca/physio/khadralab/code_BJ1.html.

62. Wiseman, P. W., C. M. Brown, …, A. F. Horwitz. 2004. Spatial mapping of integrin interactions and dynamics during cell migration by image correlation microscopy. *J. Cell Sci.* 117:5521–5534.

63. Goodsell, D.S. 2019. PDB-101: Molecule of the month: Integrin. 2011. http://pdb101.rcsb.org/motm/134.

64. Springer, T. A., J. Zhu, and T. Xiao. 2008. Structural basis for distinctive recognition of fibrinogen gammaC peptide by the platelet integrin alphaIIbbeta3. *J. Cell Biol.* 182:791–800.

65. Zhu, J., B. H. Luo, …, T. A. Springer. 2008. Structure of a complete integrin ectodomain in a physiologic resting state and activation and deactivation by applied forces. *Mol. Cell.* 32:849–861.

66. Lau, T. L., C. Kim, …, T. S. Ulmer. 2009. The structure of the integrin alphaIIbbeta3 transmembrane complex explains integrin transmembrane signalling. *EMBO J.* 28:1351–1361.

67. Wegener, K. L., A. W. Partridge, …, I. D. Campbell. 2007. Structural basis of integrin activation by talin. *Cell.* 128:171–182.

68. Hamill, K. J., S. Hiroyasu, …, J. C. R. Jones. 2015. Alpha actinin-1 regulates cell-matrix adhesion organization in keratinocytes: consequences for skin cell motility. *J. Invest. Dermatol.* 135:1043–1052.

69. Kim, D. H., and D. Wirtz. 2013. Focal adhesion size uniquely predicts cell migration. *FASEB J.* 27:1351–1361.

70. Lawson, C., S. T. Lim, …, D. D. Schlaepfer. 2012. FAK promotes recruitment of talin to nascent adhesions to control cell motility. *J. Cell Biol.* 196:223–232.

71. Velasco-Velázquez, M. A., N. Salinas-Jazmín, …, J. J. Mandoki. 2008. Reduced paxillin expression contributes to the antimetastatic effect of 4-hydroxycoumarin on B16-F10 melanoma cells. *Cancer Cell Int.* 8:8.

72. Hagel, M., E. L. George, …, S. M. Thomas. 2002. The adaptor protein paxillin is essential for normal development in the mouse and is a critical transducer of fibronectin signaling. *Mol. Cell. Biol.* 22:901–915.

73. Changede, R., and M. Sheetz. 2017. Integrin and cadherin clusters: a robust way to organize adhesions for cell mechanics. *Bioessays.* 39:1–12, Published online December 8, 2016.

74. Arnold, M., E. A. Cavalcanti-Adam, …, J. P. Spatz. 2004. Activation of integrin function by nanopatterned adhesive interfaces. *ChemPhysChem.* 5:383–388.

75. Cavalcanti-Adam, E. A., A. Micoulet, …, J. P. Spatz. 2006. Lateral spacing of integrin ligands influences cell spreading and focal adhesion assembly. *Eur. J. Cell Biol.* 85:219–224, Published online October 10, 2005.

76. Schvartzman, M., M. Palma, …, S. J. Wind. 2011. Nanolithographic control of the spatial organization of cellular adhesion receptors at the single-molecule level. *Nano Lett.* 11:1306–1312.

77. Saez, A., A. Buguin, …, B. Ladoux. 2005. Is the mechanical activity of epithelial cells controlled by deformations or forces? *Biophys. J.* 89:L52–L54.

78. Roca-Cusachs, P., A. del Rio, …, M. P. Sheetz. 2013. Integrin-dependent force transmission to the extracellular matrix by α-actinin triggers adhesion maturation. *Proc. Natl. Acad. Sci. USA.* 110:E1361–E1370.

79. Ballestrem, C., B. Hinz, …, B. Wehrle-Haller. 2001. Marching at the front and dragging behind: differential alphaVbeta3-integrin turnover regulates focal adhesion behavior. *J. Cell Biol.* 155:1319–1332.

80. Hu, K., L. Ji, …, C. M. Waterman-Storer. 2007. Differential transmission of actin motion within focal adhesions. *Science.* 315:111–115.

81. Lagarrigue, F., P. Vikas Anekal, …, M. H. Ginsberg. 2015. A RIAM/lamellipodin-talin-integrin complex forms the tip of sticky fingers that guide cell migration. *Nat. Commun.* 6:8492.

82. Cluzel, C., F. Saltel, …, B. Wehrle-Haller. 2005. The mechanisms and dynamics of (alpha)v(beta)3 integrin clustering in living cells. *J. Cell Biol.* 171:383–392.

83. Aratyn-Schaus, Y., and M. L. Gardel. 2010. Transient frictional slip between integrin and the ECM in focal adhesions under myosin II tension. *Curr. Biol.* 20:1145–1153.

84. Felsenfeld, D. P., D. Choquet, and M. P. Sheetz. 1996. Ligand binding regulates the directed movement of $\beta 1$ integrins on fibroblasts. *Nature.* 383:438–440.

85. Chang, A. C., A. H. Mekhdjian, …, A. R. Dunn. 2016. Single molecule force measurements in living cells reveal a minimally tensioned integrin state. *ACS Nano.* 10:10745–10752.

86. Van Milligen, -gnskip-->B. Ph., P. D. Bons, …, R. Sánchez. 2005. On the applicability of Fick's law to diffusion in inhomogeneous systems. *Eur. J. Phys.* 26:913–925.

87. Tupper, P. F., and X. Yang. 2012. A paradox of state-dependent diffusion and how to resolve it. *Proc. R. Soc. A Math. Phys. Eng. Sci.* 468:3864–3881.

88. Stratonovich, R. L. 1965. Fokker-planck equation with discontinuous coefficients and conditions at the surface of discontinuity. *Sov. Radiophys.* 8:500–505.

89. Pereverzev, Y. V., E. Prezhdo, and E. V. Sokurenko. 2011. The two-pathway model of the biological catch-bond as a limit of the allosteric model. *Biophys. J.* 101:2026–2036.

90. Kloeden, P. E., and E. Platen. 1992. Numerical Solution of Stochastic Differential Equations. Springer-Verlag, Berlin Heidelberg.

91. Vestergaard, C. L., and M. Génois. 2015. Temporal gillespie algorithm: fast simulation of contagion processes on time-varying networks. *PLoS Comput. Biol.* 11:e1004579.

92. Kong, F., Z. Li, …, C. Zhu. 2013. Cyclic mechanical reinforcement of integrin-ligand interactions. *Mol. Cell.* 49:1060–1068.

93. Cavalcanti-Adam, E. A., T. Volberg, …, J. P. Spatz. 2007. Cell spreading and focal adhesion dynamics are regulated by spacing of integrin ligands. *Biophys. J.* 92:2964–2974.

94. Kingma, D. P., and M. Welling. 2013. Auto-encoding variational Bayes, arXiv, arXiv:1312.6114. https://arxiv.org/abs/1312.6114.

95. Rippel, O., and R. P. Adams. 2013. High-dimensional probability estimation with deep density models, arXiv, arXiv:1302.5125. https://arxiv.org/abs/1302.5125.

96. Dinh, L., J. Sohl-Dickstein, and S. Bengio. 2016. Density estimation using Real NVP, arXiv, arXiv:1605.08803v3. https://arxiv.org/abs/1605.08803.

97. Tadavani, P. K. 2013. Nonlinear dimensionality reduction by manifold unfolding. PhD thesis. University of Waterloo.

98. Roberts, S., M. Osborne, …, S. Aigrain. 2013. Gaussian processes for time-series modelling. *Philos. Trans. A Math. Phys. Eng. Sci.* 371:20110550, Published online December 31, 2012.

99. Hastie, T., and R. Tibshirani. 1995. Generalized additive models for medical research. *Stat. Methods Med. Res.* 4:187–196.

100. Rasmussen, C. E., and C. K. I. Williams. 2006. Gaussian Processes for Machine Learning, First Edition. MIT Press, Cambridge, MA, pp. 1–248.

101. Ozair, S., and Y. Bengio. Deep directed generative autoencoders, arXiv, arXiv:1410.0630v1. https://arxiv.org/abs/1410.0630.

102. Perrone, D., and P. Favaro. 2016. A clearer picture of total variation blind deconvolution. *IEEE Trans. Pattern Anal. Mach. Intell.* 38:1041–1055.

103. Tikhonov, A. N., and V. Y. Arsenin. 1977. Solutions of Ill-Posed Problems. Winston, Washington D.C..

Biophysical Journal, Volume *117*

Supplemental Information

Dynamics of Mechanosensitive Nascent Adhesion Formation

Laurent MacKay and Anmar Khadra

Manuscript submitted to **Biophysical** *Journal*
Article

Supporting Material

Laurent MacKay[1] and Anmar Khadra[1,*]

[1]Department of Physiology, McGill University, Montreal, Quebec, Canada
[*]Correspondence: anmar.khadra@mcgill.ca

MODEL FRAMEWORK

The primary process which results in the formation of a nascent adhesion (NA) is the clustering of integrins (1). It has been suggested that very small non-specific clusters of integrin spontaneously form even in the absence of ligand binding; however, their size and spatial distributions were inconsistent with that of NAs formed in the presence of ligand binding (2). Generally speaking, in the presence of ligand, NAs were about twice as large (compared to those generated in the absence of ligand), exhibited high variability in their integrin content, and yet had a relatively restricted distribution in their size (2). This suggests that (i) there is an intrinsic clustering mechanism for integrins, (ii) ligand binding enhances this clustering mechanism to form NAs, and (iii) the area of the cluster is not directly proportional to its integrin content (i.e., there is a nonlinear relation between NA-area and the number of integrins forming it). Interestingly, it has been observed that integrins exhibit reduced diffusivity within adhesions (defined experimentally by the area underneath an adaptor protein plaque), by at least a factor of three (3). This decrease was found to be dependent on interactions with adaptor proteins through the cytoplasmic domain of integrins, suggesting that membrane-proximal adaptor proteins may exert a drag force on integrins (3). Integrins also undergo extended periods of immobilization which further decreases their lateral mobility. The frequency of long-lived immobilization is enhanced inside adhesions and has been found to be dependent on integrin's interaction with both extracellular ligands and adaptor proteins (3, 4). Thus we propose that the NA-area, as defined by the adaptor protein plaque, provides an environment within which integrin lateral mobility is decreased due to both a reduced diffusion coefficient and increased likelihood of binding to extracellular ligand.

Reduced integrin lateral mobility, due to their interactions with the adaptor protein and extracellular ligands plaque, may explain aggregation of integrins into micron-scale clusters. This, however, does not explain the presence of the adhesion plaque. Firstly, its was previously argued, from a theoretical perspective, that adhesion plaques must be self-assembling structures in order to explain the stress-induced growth of adhesions (5). Meanwhile, the adaptor protein talin and its interaction with integrins have been repeatedly found to be required for the formation of NAs (2, 6, 7). These results suggest, that the self-assembly of adhesion plaques requires both integrin and adaptor proteins to be capable of forming complexes with one another. Furthermore, increased extracellular ligand density (and thus integrin density inside the adhesion) has been shown to increase the residence time of the adaptor protein FAK inside the adhesion plaque (8). Additionally, the diffusivity of the adaptor protein paxillin shows significant heterogeneity in its value inside a single adhesion plaque, suggesting that paxillin may exist in more than one association state within the adhesion (9–11). We propose that adaptor proteins form membrane-proximal aggregates around a seed of a small number of integrins, and that subsequent retention of integrins inside the adhesion area (as discussed above) allows for growth of the adhesion plaque due to the decreased mobility of adaptor proteins. This decreased mobility manifests itself in the model as a decrease in the off-rate of adaptor proteins in the presence of integrins. The precise nature of the mechanism which reduces the off-rate will depend on the specific adaptor protein in question. In the model developed herein, we generically describe it as a reversible tethering to the membrane by integrin.

Together, these effects constitute a mechanism for the self-aggregation of cytoplasmic adaptor proteins and integrins, a phenomenon we refer to hereafter as co-aggregation. More specifically, we propose that (i) integrin lateral mobility is modulated locally by the presence of membrane-proximal adaptor proteins, and (ii) adaptor proteins are effectively tethered to the membrane by integrins. In this manner, the presence of a protein of one type increases the probability that a protein of the other type will be present in close proximity. This positive feedback between the two types of proteins would allow them to serve as templates for one another in the formation of membrane-proximal aggregates of adaptor protein (i.e., an adhesion plaque). We incorporate this mechanism into a mathematical model that satisfies the following assumptions (see Fig. 1A):

1. Adaptor proteins are modeled as either being in a well-mixed cytosolic bulk phase or in a spatially confined region $\Omega(t) \in \mathbb{R}^2$ which delimits the adhesion. Their density ρ inside NAs (i.e., the domain Ω) is assumed to be uniform. Furthermore, we impose the conservation of matter by assuming that the adaptor protein content of a NA is drawn from a

finite reservoir of N_P adaptor proteins, and therefore the number of cytosolic adaptor proteins N_{cyto} is given by

$$N_{cyto} = N_P - \rho A, \tag{S1}$$

where $A := \|\Omega\|$ is the surface area of the adhesion plaque. This means that, as NAs grow very large, they will deplete the cytoplasmic pool of adaptor proteins until an equilibrium between their growth and shrinkage rates is reached. When adaptor proteins are in the adhesion plaque, they can either be associated with the rest of the adaptor protein scaffold or they may be bound to an integrin receptor where they become reversibly tethered to the membrane. We assume that individual adaptor proteins leave the adhesion at a rate k_{off} and $(1-\delta)\,k_{off}$, where $\delta \in (0,1)$, when they are untethered and tethered to integrin, respectively. This difference in off-rate in the presence of integrins is what leads to the aggregation of adaptor proteins around integrins.

2. We model integrins as 2-dimensional (2D) Brownian particles that diffuse freely outside the adhesion, and exhibit reduced mobility within the adhesion domain Ω. This reduced mobility is implemented through two biophysical mechanisms. In the first, we assume that the diffusion coefficient of integrins is lower when they are underneath the adhesion plaque, i.e.,

$$D(x) = \begin{cases} D_{in} & x \in \Omega \\ D_{out} & \text{otherwise} \end{cases}, \tag{S2}$$

where $D_{in} \leq D_{out}$ are the diffusion coefficients inside and outside the adhesion domain Ω, respectively (3). In the second, we make the simplifying assumption that only the adhesion environment provides the necessary ingredients for the long-lived immobilization of integrin, which we attribute to ligand binding (3). Therefore, we assume that integrins inside Ω may bind to an extracellular ligand and become reversibly immobilized with a binding affinity K_{bind}.

Spatial Assumptions

We consider a periodic array of adhesions on a square lattice with an inter-adhesion spacing h. This simplifying assumption of periodicity allows us to study the problem on a small $h \times h$ square patch of membrane that is assumed to receive no net flux of matter from adjacent patches (see Fig. 1B) because they are all in equilibrium. We further consider that the $h \times h$ square patch contains N_I integrins and sits under the adhesion plaque consisting of N_P adaptor proteins. Integrins are assumed to diffuse in a 2-dimensional plane (i.e., the membrane), and a circular aggregation of adaptor proteins centered at the origin with an area A that delimits the region defining the adhesion plaque (i.e., $\Omega = \left\{(x,y) : \pi\left(x^2+y^2\right) \leq A\right\}$).

Integrin Reaction-Diffusion Model

In order for the force transmission through an adhesion to the ECM to be effective, its integrins must bind to their extracellular ligands. When bound to their ligand, integrins exhibit a diverse range of mobilities (3, 12, 13). Generally, we can expect the integrins to have a reduced mobility upon binding to ligand. We consider the extreme case of complete immobilization in order to understand what can be expected at most from the ligand binding process. Within an adhesion, only a certain proportion of integrins are bound to ligand (3, 4, 14). We denote the total number of integrins inside the adhesion area by N_{in}, while L_{in} and M_{in} denote the number of liganded and mobile integrins, respectively (i.e., $N_{in} = L_{in} + M_{in}$). If we assume that ligand-binding induced immobilization happens only within the adhesion, then the dynamics of M_{in} is given by

$$\dot{L}_{in}(t) = k_{unbind}\left(K_{bind} M_{in} - L_{in}\right) := R_{bind},$$

where k_{unbind} is the unbinding rate of an integrin, and K_{bind} is its binding affinity, given by

$$K_{bind} = \frac{k_{bind}}{k_{unbind}},$$

with k_{bind} denoting the first order binding rate of a single integrin (assuming fixed extracellular ligand density). In order to account for variations in the density of extracellular ligand, denoted $\left[\text{Ligand}\right]$, we use the expression

$$k_{bind} = \overline{k}_{bind}\left[\text{Ligand}\right], \tag{S3}$$

where $\overline{k}_{bind}$ is a the second order binding rate.

An unbound integrin is assumed to diffuse freely in the cellular membrane. We use the Fokker-Planck (FP) diffusion equation to describe the spatiotemporal evolution of the unbound integrin density $I(x)$. Such a model has a local flux $j(x)$, given by

$$j(x) = \nabla \left(D(x) I(x) \right), \tag{S4}$$

where ∇ is the gradient operator and $D(x)$ is the diffusion coefficient. In situations with inhomogeneous diffusion coefficient, such as Eq. S2, this FP flux equation is more applicable than the more widely used Fick's law (15). We are interested in the time-invariant (equilibrium) behaviour of the adhesion; we therefore assume zero-flux boundary conditions on the outer edge of the membrane patch. This corresponds to finding a solution where the flux is zero everywhere. For a piecewise constant diffusion coefficient, such a solution is expected to be piecewise constant at equilibrium, given by

$$I(x) = \begin{cases} I_{in} & x \in \Omega \\ I_{out} & \text{otherwise,} \end{cases}$$

where I_{in} (I_{out}) is the density of unbound integrins inside (outside) the adhesion (16). However, the discontinuity in Eq. S2 leads to to a singular flux at the interface between the adhesion plaque boundary and the rest of the membrane, given by

$$j_0 = (D_{out} I_{out} - D_{in} I_{in}) \hat{r},$$

where $\hat{r}$ is the radial unit vector (17). As time tends towards infinity, diffusion smooths out all concentration gradients such that the non-singular portion of the flux in Eq. S4 becomes zero irrespective of the integrin densities in and out of the adhesion. Therefore, near equilibrium, we take the total flux of free integrins into the adhesion due to diffusion to be the integral along the interface of the singular component of the flux

$$J_{in} = \int_0^{2\pi} j_0 \cdot \hat{r} r d\theta = (D_{out} I_{out} - D_{in} I_{in}) 2\pi r,$$

where r is the radius of the adhesion. We note that $I_{in} = M_{in}/A$ and thus, by imposing conservation of matter, we eliminate the variable I_{out} to obtain the relation $I_{out} = (N_I - N_{in})/(h^2 - A)$. Finally, the rate of change of unbound integrins inside the adhesion is given by the difference between the integrated diffusive flux and the binding reaction rate, i.e.,

$$\dot{M}_{in} = J_{in} - R_{bind}. \tag{S5}$$

We have assumed in the derivation of Eq. (S5) that diffusion reaches its equilibrium within NAs. Although it is often assumed that NAs are far from equilibrium due to their short stability period (18–21), recent evidence suggests that conditions preventing NA-disassembly produces integrin clusters with very similar properties (in terms of number and size) to those that do disassemble (2). This indicates that NAs come very close to their equilibrium before disassembling, and motivates the treatment of integrin dynamics near the equilibrium of the diffusion process in this study.

Adhesion Plaque Adsorption Model

To capture the kinetics of adaptor protein aggregation into a membrane-proximal plaque, we adapt the "Bulk-on/Bulk-off" model of adsorption (22), where adhesions are assumed to be able to grow (shrink) from any point in its interior by addition (subtraction) of adaptor proteins that are incorporated into the adhesion with a uniform density ρ. Adaptor proteins are assumed to be added to an adhesion at a rate

$$\gamma(A) = A k_{on}^0 P_{out}, \tag{S6}$$

where $P_{out} = \frac{N_{cyto}}{h^2}$ is the density (per unit area) of free adaptor proteins. Furthermore, we consider that integrins inside the adhesion stabilize the adhesion plaque leading to less adaptor proteins leaving the adhesion per unit time. In the model, this is implemented by assuming that adaptor proteins can exist in two states within the adhesion, one which is reversibly tethered to the membrane by integrins and the other loosely associated with adjacent adaptor proteins. Adaptor proteins can leave the adhesion plaque with a rate k_{off} and $(1-\delta) k_{off}$ for the untethered and tethered states, respectively. Assuming that fast kinetics govern the association of integrins and adaptor proteins within the adhesion, we prescribe a phenomenological Hill-function expression for the off-rate of an adaptor protein, given by

$$\kappa\left(N_{in}/A\right) = k_{off}\left((1-\delta) + \delta \frac{b^n}{b^n + \left(N_{in}/A\right)^n}\right), \tag{S7}$$

where N_{in}/A is the total integrin density in the adhesion, k_{off} is the maximal observed degradation rate of the adhesion, δ is the magnitude of the co-aggregation between integrins and adaptor proteins (a value of 0 indicating no co-aggregation while a value of 1 indicating full co-aggregation), n is the degree of cooperativity between integrins for the tethering of adaptor proteins ($n = 1$ indicates no cooperativity while $n > 1$ indicates positive cooperativity), and b is the integrin density needed to tether 50% of adaptor proteins. Based on this, we obtain the following dynamic equation for adhesion area

$$\frac{dA}{dt} = \frac{1}{\rho}\left(\gamma(A) - A\rho\kappa(I_{in})\right) = A\left[\frac{k_{on}^0 P_{out}}{\rho} - \kappa\left(N_{in}/A\right)\right].$$

Geometric Constraints

The complete set of equations governing NA dynamics are given by Eqs. 1a-1c (see main text). The equilibria of the system lie at the intersection of its nullsurfaces. The plane $A = 0$ is one of the A-nullsurfaces, while

$$L_{in}^* = K_{bind} M_{in}^* \tag{S8}$$

is the L_{in}-nullsurface, and

$$M_{in}^* = \frac{A^* C_I K_{in} h^2}{A^*\beta + h^2} \tag{S9}$$

is the M_{in}-nullsurface, where $K_{in} = D_{out}/D_{in}$ and $\beta = \left(K_{in}(1 + K_{bind}) - 1\right)$. At the intersection of these nullsurfaces, we have the steady state $\mathbf{Z} = (A, M_{in}, L_{in}) = (0, 0, 0)$, representing the unclustered configuration of adhesion proteins (with both adaptor proteins and integrin receptors uniformly distributed in space). The second A-nullsurface (see Eq. 2) forms with the other nullsurfaces a steady state where adhesion proteins are co-aggregated into a dense cluster. The conditions which cause the system to switch between the unclustered and the clustered steady states are analyzed in the main text. Nonetheless, from Eq. S9, we can see that $N_{in} \to \infty$ as $C_I \to \infty$ provided that $A \neq 0$. In this limit, integrins have their maximum effect on the aggregation of adaptor proteins, and thus the clustered steady state will reach some maximum area A^∞. According to the second term in Eq. 1a, this maximum area is given by

$$A^\infty := h^2\left(\frac{C_P}{\rho} - \frac{1-\delta}{K_{on}}\right), \tag{S10}$$

where $K_{on} = k_{on}^0/k_{off}$. The first term in Eq. (S10) is the maximal fractional area the adhesion plaque can attain if all adaptor proteins become stuck to the membrane, while the second term is a correction factor that accounts for the finite binding affinity of adaptor proteins being absorbed into the plaque. This indicates that A^∞ depends linearly on the adaptor protein density, and remains finite regardless of the integrin density. It is important to consider the geometric assumptions of our model, in order to ensure that its predictions are physically meaningful. By letting $\phi = [(C_P/\rho) - ((1-\delta)/K_{on})]$, we obtain $A^\infty = h^2\phi$. For a circular adhesion lying strictly within a square lattice cell, we must have $\phi \in \left[0, \pi/4\right)$ in order for the results of our model to remain biophysically relevant.

Generally, if we were to formulate this model for some other lattice with a unit cell area A_{max} (e.g., $A_{max} = h^2$ for the square lattice), we can adapt all our results by replacing h^2 with the particular value of A_{max}. In such a case, the upper bound on ϕ will depend on the geometry of the lattice and the adhesion; however, in general, we will always have $\phi < 1$ as a maximum upper bound. For $\phi \geq 1$, our circular adhesions will take up more area than is available for the given lattice, and thus the membrane will be saturated with adhesion plaque on the length scale h. Because ϕ is independent of the lattice geometry, we interpret this upper bound as being set by the biophysical and chemical properties of the proteins involved rather than an artifact of the periodic lattice assumption.

Transcritical Bifurcation

The switch between the unclustered $\mathbf{Z} = (0, 0, 0)$ and clustered $\mathbf{S}^* = \left(A^*, M_{in}^*, L_{in}^*\right)$ steady states occurs at a transcritical bifurcation point. In what follows, we analyze the stability properties of this steady state. As discussed in the main text, for simplicity we focus on the case $n = 1$. Under these conditions, the Jacobian matrix of the system evaluated at the unclustered steady state has three eigenvalues, two of which are strictly negative and one that can change its sign, given by

$$\lambda_1 = k_{on}^0\left(\phi - \frac{b\delta}{bK_{on} + \hat{C}_I}\right).$$

Hence, the unclustered steady state is unstable if $\lambda_1 > 0$. A switch in the sign of λ_1 can occur when certain parameters of the model cross a threshold. For the intracellular densities C_I and C_P, these thresholds are given by

$$C_I > C_I^{\ddagger} := \frac{b\left(\delta - \phi K_{on}\right)}{\phi K_{on} K_{in}\left(1 + K_{bind}\right)} \tag{S11}$$

and

$$C_P > C_P^{\ddagger} := \frac{\rho\left(b + K_{in}\left(1 + K_{bind}\right) C_I\left(1 - \delta\right)\right)}{K_{on}\left(b + K_{in}\left(1 + K_{bind}\right) C_I\right)} \geq 0, \tag{S12}$$

respectively. Moreover, the threshold for the binding affinity K_{bind} is given by

$$K_{bind} > K_{bind}^{\ddagger} := \frac{b\delta - \phi K_{on}\left(b + C_I K_{in}\right)}{\phi C_I K_{in} K_{on}}$$

which, according to Eq. S3, can produce the following threshold for ligand concentration

$$\left[\text{Ligand}\right] > \left[\text{Ligand}\right]^{\ddagger} := \frac{k_{unbind}}{\overline{k}_{bind}} \frac{b\delta - \phi K_{on}\left(b + C_I K_{in}\right)}{\phi C_I K_{in} K_{on}}. \tag{S13}$$

Once the system passes through the transcritical bifurcation, the model gives birth to the clustered steady state $\mathbf{S}^*$ representing a stable adhesion plaque with area A^* that contains $N_{in}^* = M_{in}^* + L_{in}^*$ integrins.

Integrin Mechanosensitivity

Integrin mechanosensitivity is thought to arise from mechanically-induced conformational changes. It has been suggested that the mechanical extension and separation of the extracellular legs of integrin receptors results in a long-lived bound state (23, 24). We incorporate these ideas into our model as a force-dependent ensemble average lifetime $\left\langle \tau\left(f\right)\right\rangle$, where f is the force applied on the integrin. This is modeled using the two-pathway model of bond-dissociation (25), given by

$$\left\langle \tau\left(f\right)\right\rangle = \tau_0\left(de^{\hat{f}(c+d)} + c\right) \frac{1}{ce^{fd} + de^{\hat{f}(c+d)}e^{-cf}}, \tag{S14}$$

where τ_0 is the bond lifetime with zero applied force, $\hat{f}$ is the force which optimizes the bond lifetime, and $c, d > 0$ are coefficients. These coefficients are determined numerically by first setting

$$d = \frac{c\hat{\tau}}{\tau_0 e^{c\hat{f}} - \hat{\tau}} + \frac{1}{\hat{f}} \times W\left(-\frac{c\hat{f}\tau_0 e^{-\frac{c\hat{f}\hat{\tau}}{\tau_0 e^{c\hat{f}} - \hat{\tau}}}}{\tau_0 e^{c\hat{f}} - \hat{\tau}}\right),$$

where $\hat{\tau} = \left\langle \tau\left(\hat{f}\right)\right\rangle$ is the optimal bond lifetime and $W\left(\cdot\right)$ is the W-Lambert function, followed by varying c in such a way that $\left\langle \tau\left(60\,\text{pN}\right)\right\rangle \approx 0.1$ s (see Fig. S1 for profile and Parameter Estimation for numerical values). Finally, this give the numerical expression

$$\left\langle \tau\left(f\right)\right\rangle = \frac{1}{0.666667exp(-0.0876215F) + 6.60165 \times 10^{-8}\exp(0.313789f)} \tag{S15}$$

In order to incorporate the mechanosensitive properties of integrins into our binding model, we set the integrin unbinding rate k_{unbind} to be the reciprocal of $\left\langle \tau\left(f\right)\right\rangle$, the ensemble bond lifetime. This means that

$$K_{bind} = k_{bind}\left\langle \tau\left(f\right)\right\rangle, \tag{S16}$$

(i.e., all bound integrins are assumed to bear an equal load). The numerical value of f is determined by assuming that the NA experiences a fixed stress (force per unit area), given by

$$\sigma = \frac{fL_{in}}{A}. \tag{S17}$$

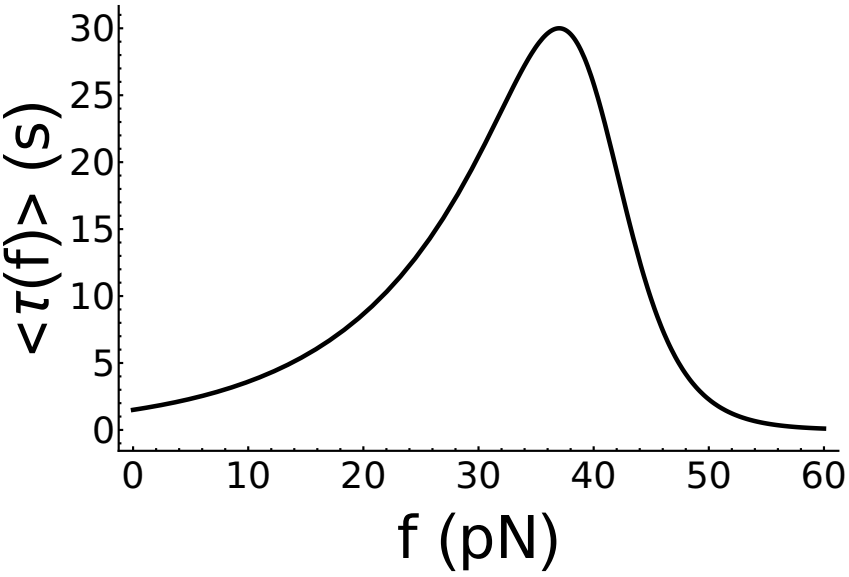

Figure S1: Integrin-ligand bond lifetime, $\langle \tau(f) \rangle$, as a function of f, the applied force per integrin. The biphasic profile resembles that obtained for catch bonds between integrin and fibronectin (26).

Stochastic Simulations

We note that the integrin flux described by Eq. S5 is only valid for small perturbations around the steady state as it neglects the effects of concentration gradients. In order to more accurately capture the full integrin dynamics specified in Eq. S4 far from equilibrium, we re-formulate our model as a discrete system, where we use a master equation approach to describe the aggregation of adaptor proteins at the adhesion plaque and the reversible binding of integrins within the adhesion region. Furthermore, to account for the diffusion of integrins along the membrane, we use a Brownian dynamics approach where each integrin is given a position $\vec{x}(t)$ that evolves in time according to a Brownian motion with local diffusivity given by Eq. S2, and use the Euler-Maruyama update scheme to obtain the time-dependent positions of integrins (27). By denoting the number of adaptor proteins in the adhesion plaque by i, we obtain the following total number of integrins $\nu(t)$ inside a NA of area $A = i/\rho$

$$\nu(t) = \sum_{k=1}^{N_I} \begin{cases} 1 & \text{if } \pi \vec{x}_k(t) \cdot \vec{x}_k(t) \leq i/\rho \\ 0 & \text{otherwise,} \end{cases}$$

where $\vec{x}_j(t)$ is the position of the j^{th} integrin at time t. Setting p_i to be the probability of having a NA with i adaptor proteins, we conclude that the aggregation of adaptor proteins at the adhesion plaque obeys a master equation, given by

$$\rho \dot{p}_i(t) = \left(g_{i-1} p_{i-1} + s_{i+1}(\nu(t)) p_{i+1}\right) - \left(g_i + s_i(\nu(t))\right) p_i, \tag{S18}$$

where g_i (s_i) is the growth (shrinkage) reaction-rate, defined by $g_i = \gamma(i/\rho)$ and $s_i(\nu) = i\kappa(\rho\nu/i)$, respectively. Letting ℓ_j be the probability of having j bound integrins inside the adhesion, we obtain the following master equation for binding kinetics of integrin

$$\dot{\ell}_j(t) = k_{bind}\left(\nu(t) - (j-1)\right)\ell_{j-1} + (j+1)k_{unbind}\ell_{j+1} - \left(k_{bind}\left(\nu(t) - j\right) + jk_{unbind}\right)\ell_j. \tag{S19}$$

When integrins become bound, we reversibly set their diffusion coefficient to zero, and set their unbinding rate to $k_{unbind} = \langle \tau(i\sigma/\rho j) \rangle^{-1}$. The time-course of the chemical reactions is realized through a temporal Gillespie algorithm, that allows for efficient stochastic simulations of reactions with time-dependent propensities (28). This is necessary to account for the fact that both reactions have propensities which depend on $\nu(t)$, and that integrins may diffuse into or out of the adhesion independently of the reactions governed by Eqs. S18 or S19.

Parameter Estimation

Model parameter values are inferred, when possible, using algebraic expressions from the model equated to values obtained from experimental measurements. In the main text, we have identified two regions of interest in parameters space, which we

have denoted regions 2 & 3. The assumptions inherent in each region leads to slightly different algebraic expressions for model parameters. We begin by discussing the expressions that the two regions have in common, followed by explaining the distinct approaches used in each region.

Firstly, we introduce the relative enrichment of integrins inside the adhesion E, which has been observed to be in the range of $E \in [2, 12]$ in various physiological conditions (3, 29). Using the conservation of matter for integrins, we obtain the following expression for their density

$$C_I = \frac{I_{in}\left(A_1 + \left(h^2 - A_1\right)/E\right)}{h^2}, \tag{S20}$$

where I_{in} is the density of integrins inside the adhesion, A_1 is the mean area of NA (to be estimated from experimental measurements), and h is the mean inter-adhesion spacing. The parameter h is determined using

$$\bar{N}^*_{in} := \lim_{K_{bind}\to\infty} M^*_{in} + L^*_{in} = C_I h^2$$

which can be combined with Eq. (S20) to yield

$$h = \left(A_1\left(1 - E\right) + E\frac{N_2}{I_{in}}\right)^{1/2}, \tag{S21}$$

where N_2 is the number of integrins in a NA when integrin binding is very strong (also to be determined from experimental measurements). Secondly, an expression for the parameter b can be obtained by solving $I_{in} = N^*_{in}/A^*$, with $N^*_{in} = L^*_{in} + M^*_{in}$, to obtain

$$b = \frac{I_{in}K_{on}\left(-(\beta+1)C_I + \beta\phi I_{in} + I_{in}\right)}{(\beta+1)C_I K_{on} - I_{in}\left(-\beta\delta + \beta\phi K_{on} + K_{on}\right)}, \tag{S22}$$

where the estimation of the parameters K_{on} and K_{in} (implicit in β) must be dealt with differently in the two regions. We may also use the model steady states to derive the expression

$$E = \frac{N^*_{in}/A^*}{\left(N_I - N^*_{in}\right)/\left(h^2 - A^*\right)} = \left(1 + K_{bind}\right)K_{in}$$

which may be rewritten as an expression for the binding affinity, given by

$$K_{bind} = \frac{E}{K_{in}} - 1. \tag{S23}$$

The parameter δ is estimated by considering the ratio of FRAP recovery times of the intermediate and slow fractions of the adaptor protein paxillin and vinculin within focal adhesions (10). This ratio is in the range of 20-80, corresponding to a value of $\delta \in [0.95, 0.99]$. We also estimate the value of the mean density of adaptor proteins prior to adhesion formation, C_P, using the literature value of paxillin concentration $[\text{paxillin}] \approx 2.3\,\mu$M multiplied by an estimate of cell volume $V_{cell} \approx 1000\,\mu\text{m}^3$ to get the total number of paxillin molecules in the cell $N_{pax} \approx 1.38 \times 10^6$ (30). We then use the simple approximation $C_P \approx N_{pax}/A_{cell} = 8050\mu\text{m}^{-2}$, where $A_{cell} \approx 172\,\mu\text{m}^2$ is the estimated cell area determined from analysis of imaging data (2), to obtain $C_P \approx 8050\,\mu\text{m}^{-2}$. Finally, the parameters k_{off} and ρ are chosen in such a way that stochastic simulations of adhesion disassembly/assembly have a timescale and stochasticity comparable to that observed experimentally (19), respectively.

Region 3

From a super-resolution quantification of adhesion size and integrin content (2), we can obtain the following estimates $I_{in} \approx 6600\,\mu\text{m}^{-2}$ and $A_1 \in [7, 9] \times 10^{-3}\,\mu m^2$. The integrin clusters produced by the same study (2), upon exposing cells to Mn^{+2} (which switches integrins into a high-affinity state), can be used to obtain the estimate $N_2 \approx 75$. Using Eq. (S21), with $E \approx 12$ (i.e., by assuming that NAs are among the most enriched in integrins) and $A_1 \approx 8.7 \times 10^{-3}\,\mu m^2$, we obtain $h \approx 0.2\,\mu m$. This estimate is further verified visually by analyzing the spacing between NAs in images (2). Furthermore, region 3 is differentiated from region 2 by the fact that it produces adhesions even in the absence of ligand binding. Experimentally, in the absence of ligand, it was found that small clusters of integrin containing $N_3 \in [4, 19]$ integrins form with an area $A_3 \in [1, 4.4] \times 10^{-3}\mu m^2$ (2). We use these quantifications to aid us in our parameter estimation by setting them equal to appropriate model steady states, i.e., by letting

$$N_3 = \tilde{M}^*_{in} + \tilde{L}^*_{in} \tag{S24}$$

Table S1: Auxiliary parameter values used in the determination of model parameters (see Table S3 for model parameter values).

Symbol	Definition	Estimated Value	Reference(s)
E	Fold-enrichment of integrins within the adhesion	12	(3, 29)
I_{in}	Mean density of integrins within the adhesion	6600 μm^2	(2)
A_1	Mean NA-area	8.7×10^{-3} μm^2	(2)
N_2	Number of integrins inside NAs when Mn^{2+} is added to extracellular medium	75	(2)
$[\text{paxillin}]$	Physiological paxillin concentration	2.3 μM	(30)
V_{cell}	Volume of a mouse embryonic fibroblast (MEF) cell	1000 μm^3	-
A_{cell}	Area of a MEF cell	172 μm^2	(2)
N_3	Number of integrins inside NAs in the absence of extracellular ligands	6	(2)
A_3	Mean NA-area in the absence of extracellular ligands	2.7×10^{-3} μm^2	(2)
$\langle\tau\,(0\,\text{pN})\rangle$	Ensemble average of integrin-ligand bond lifetime in the absence of force	1.5 s	(26)
$\langle\tau(\hat{f})\rangle$	Ensemble average of the optimal integrin-ligand bond lifetime	30 s	(31)
$\hat{f}$	The force that optimizes bond lifetime	37 pN	(26)
$\langle\tau\,(60\,\text{pN})\rangle$	Ensemble average of the integrin-ligand bond at very large forces	0.1 s	(26)

and

$$A_3 = \tilde{A}^*. \tag{S25}$$

These two expressions are then used in conjunction with Eqs. (S20), (S22), and (S23) to yield

$$K_{in} = \frac{N_3\left(\left(A_1(E-1)+A_3\right)I_{in} - EN_2\right)}{A_3\left(N_3-N_2\right)I_{in}} \approx 1.2, \tag{S26}$$

$$K_{on} = \frac{\delta\left(\frac{EN_2}{I_{in}} - A_1(E-1)\right)\left(A_3\left(A_1-A^\infty\right)I_{in} + N_3\left(A^\infty - A_3\right)\right)}{\left(A^\infty-A_1\right)\left(A^\infty-A_3\right)\left(N_3-A_3I_{in}\right)} \approx 0.70, \tag{S27}$$

$$K_{bind} = \frac{\left(A_1-A_3\right)(E-1)N_3I_{in} + EN_2\left(A_3I_{in}-N_3\right)}{N_3\left(EN_2 - \left(A_1(E-1)+A_3\right)I_{in}\right)} \approx 8.8, \tag{S28}$$

and

$$b = \frac{A_3I_{in}\left(A^\infty - A_1\right) + N_3\left(A_3 - A^\infty\right)}{\left(A_1-A_3\right)A_3}, \tag{S29}$$

where we have used $\delta \approx 0.97$, $A_2 \approx 2.7\times10^{-3}$ μm^2, and $N_3 \approx 6$ (b remains to be determined). The parameter A^∞ is determined from data. More specifically, using the *maximum a posteriori* (MAP) estimate of the relation between adhesion area and its integrin content (see dotted line in Fig. 2). This data is fit to the A-nullcline given by Eq. (2) using a nonlinear least squares approach and taking Eq. (S29) into consideration . The values of the fit parameters and their 95% confidence bounds are provided in Table S2. The confidence interval on the quantities b and A_0 are relatively large, indicating that they are not well constrained by the data at hand. Nonetheless, these confidence intervals do not contain zero and only cover one order of magnitude, so we deem them to be acceptable. This completes model parameter estimation in Region 3 necessary to generate quantitative understanding of the model developed in this study.

Region 2

Region 2 ($[\text{Ligand}]^\ddagger > 0$) can be distinguished from region 3 ($[\text{Ligand}]^\ddagger < 0$) by the fact that NAs will not form in the absence of ligand. As discussed in the main text, the transition from region 2 to region 3 may be achieved by decreasing K_{on}. We therefore keep the numerical values of all other parameters determined in region 3 as is, and use a different formalism for

Table S2: Least-squares estimates of model parameters and confidence intervals obtained from a nonlinear least squares fitting of the A-nullcline to data.

Symbol	Least-Squares Estimate	95% Confidence Interval
A^{∞}	$0.0124\,\mu\text{m}^2$	$[0.0118, 0.0129]\ \mu\text{m}^2$
b	$463\,\mu\text{m}^{-2}$	$[68.8, 806]\ \mu\text{m}^{-2}$
A_0	-0.038	$[-.0204, -0.239]\ \mu\text{m}^2$

determining K_{on}. More precisely, we use Eqs. (S13), (S20), and (S21) to obtain

$$K_{on} = \frac{b\delta\left(EN_2 - A_1(E-1)I_{in}\right)^2}{A^{\infty}I_{in}\left(N_2\left(bE + I_{in}K_{in}\left([Ligand]^{\ddagger}\frac{\bar{k}_{bind}}{k_{unbind}} + 1\right)\right) - A_1 b(E-1)I_{in}\right)}, \tag{S30}$$

where we have used previous experimental finding to estimate $\left[\text{Ligand}\right]^{\ddagger} \approx 200\mu m^{-2}$, and the ratio $\bar{k}_{bind}/k_{unbind} = 0.005$ was chosen such that the equilibrium of NA-area $A^* \approx A^{\infty}$ for ligand densities given by $\left[\text{Ligand}\right] \geq 10,000\,\mu\text{m}^{-2}$ (see Fig. 3 in main text) as suggested by the spreading behaviour of cells when cultured on substrates with variable ligand density (32, 33)

Mechanosensitivity of Integrin

The coefficients in Eq. S14 are determined based on atomic force microscopy data on the bond lifetime of integrins (26, 31). More specifically, we have $\left\langle \tau\left(0\,\text{pN}\right)\right\rangle = 1.5$ s, $\langle\tau\rangle$ has a maximum at 37 pN, $\left\langle \tau\left(37\,\text{pN}\right)\right\rangle = 30$ s, and $\left\langle \tau\left(60\,\text{pN}\right)\right\rangle = 0.1$ s. Using these values, the coefficients $d \approx 0.32$ and $c \approx 0.088$ that appear in Eq. (S14) are determined (as discussed before) algebraically and by numerical optimization, respectively.

CONDITIONAL EXPECTATION ANALYSIS

Introduction

In numerous scientific applications, quantitative measurements of a system near a quasi-equilibrium are made and then analyzed. Rather than providing a precise description of a system, we may assume that it can be (at least partially) described by a set of measurements (e.g., a population may be described by the body temperature of its individuals, or a macro-molecular complex may be described by its mass and charge). Let us consider the simple experimental scenario in which measurements of two quantities of interest X and Y are made. These may represent the same quantity in two different conditions or two different quantities in the same condition. If there is a relation between the two measurements X and Y due to the intrinsic interactions of the system under study, one may attempt to derive this relation from experimental data. However, this task is complicated by the presence of stochastic fluctuations, measurement error, heterogeneity between realizations, and large data sets. With this in mind, let us consider a pair of correlated random variables (X, Y) measured simultaneously from a dynamical system near a unique equilibrium $\left(\bar{X}, \bar{Y}\right)$ using a homoscedastic model

$$(X, Y) = \left(\bar{X}, \bar{Y}\right) + (\chi, \gamma)\,,$$

where χ (along with γ) is an independent identically distributed additive noise. If both quantities X and Y have an effect on the dynamics of the physical system being observed, the equilibrium $\bar{Y}$ can be expressed as

$$\bar{Y} = f\left(\bar{X}\right). \tag{S31}$$

Given samples of (X, Y), collected under a variety of experimental conditions, it may not be straight-forward to estimate $f(\cdot)$ if the values of the corresponding $\left(\bar{X}, \bar{Y}\right)$ cannot be readily determined. This situation may arise when studying phenomena at the sub-cellular level, due to high levels of both intracellular and inter-cellular heterogeneity present even when the experimental

Table S3: Model parameter values used in the numerical simulations. Parameter values are obtained either directly from the literature or estimated analytically using model-derived equations as indicated in columns labelled source. Parameter values and sources which are different in region 3 are in parentheses.

Symbol	Definition	Value Region 2 (Region 3)	Source Region 2 (Region 3)
δ	Fractional decrease in adaptor protein off-rate (k_{off}) when tethered by integrin.	0.97	Ref. (10)
b	Integrin density inside adhesion which tethers 50% of adaptor proteins	463 μm^{-2}	Eq. (S29)
C_I	Mean density of integrins in the membrane	1844 μm^{-2}	Eq. (S20) ’
h	Mean distance between adhesions	0.20 μm	Eq. (S21)
K_{in}	D_{out}/D_{in}	1.22	Eq. (S26)
D_{out}	Diffusion coefficient of integrin outside the adhesion	0.28 μm^{2}s^{-1}	Refs. (3, 4)
D_{in}	Diffusion coefficient of integrin inside the adhesion	0.22 μm^{2}s^{-1}	$K_{in} = \frac{D_{out}}{D_{in}}$
K_{on}	Affinity of adaptor protein adsorption reaction in the absence of integrins	0.29 (0.7)	Eq. (S30) (Eq. (S27))
k_{off}	Adaptor protein off-rate in the absence of integrins	1.0 s^{-1}	-
k_{on}^0	Kinetic parameter governing on-rate for adsorption of adaptor proteins into the adhesion plaque††	0.31 s^{-1} (0.73 s^{-1})	$K_{on} = \frac{k_{on}^0}{k_{off}}$
ρ	Density of adaptor proteins in the adhesion plaque	4000 μm^{-2}	-
ϕ	Maximum fractional area of a NA	0.30	Least-Squares
C_P	Basal density of adaptor proteins in the cytosol	8050 μm^{-2}	Ref. (30)
K_{bind}	Binding affinity of single integrins	8.81	Eq. (S28)
k_{bind}	Binding rate of single integrins (= $\overline{k}_{bind}$[Ligand])	2.58 s^{-1}	$k_{bind} = \frac{K_{bind}}{\langle \tau(0\,\mathrm{pN}) \rangle}$

†† In order to obtain an estimate of the first order reaction rate for a bi-molecular adaptor protein binding event, we can use Eq. (S6) with $A = \rho^{-1}$ and $P_{out} = C_P$. This yields binding rate estimates of 0.62 s^{-1} and 1.5 s^{-1} in regions 2 and 3, respectively.

conditions are fixed. In order to circumvent this difficulty, we employ the probability distributions of X and Y instead. Assuming that χ (γ) is independent of $\bar{X}$ ($\bar{Y}$), we can compute the observed probability density of X (Y) as

$$\begin{aligned} P_X &= P_{\bar{X}} * P_{\chi}, \\ P_Y &= P_{\bar{Y}} * P_{\gamma}, \end{aligned}$$

where $*$ denotes the convolution operator. Assuming that f is a monotonic function, the the probability distribution of $\bar{Y}$ is related to that of $\bar{X}$ by the *change of variable equation,* given by

$$P_{\bar{Y}}(f) = P\left(\bar{Y} = y \,|f\right) = \frac{P_{\bar{X}}(x)}{|f'(x)|}, \tag{S32}$$

where f' is the derivative of f and x is the pre-image of y (i.e., $x = f^{-1}(y)$).

Experimentally, one may repeatedly measure both X and Y and approximate the marginal distributions P_X and P_Y by binning data to make the histograms $\mathbf{P_X}$ and $\mathbf{P_Y}$, respectively. In what follows, we will explain a methodology for determining f from these histograms.

Relation to Previous Work

The task of deducing a transformation $f(\cdot)$ from data is central to numerous machine learning techniques. However, these techniques differ in their motivation from the data analysis task we have presented above. For example, in the unsupervised learning methods of density estimation and manifold learning/unfolding the transformation f is used to more efficiently represent data in a so-called representation space, which is useful when dealing with very high dimensional data (34–37). Such methods assume that P_X is unknown and use well known parametric distributions as a prior on X in their inference of f. Such

approaches are inappropriate for our needs as they ignore the data $\mathbf{P_X}$, and thus it is unlikely that the inferred f would satisfy Eq. (S32). Alternatively, Gaussian Process models and Generalized Additive Models have both been used in supervised learning tasks to infer relationships between experimentally measured variables X and Y (38–40). However, these approaches require pairing of the data into coordinates (X, Y), which may not always be possible. On the other hand, our approach requires only knowing the marginal distributions $\mathbf{P_X}$ and $\mathbf{P_Y}$ which may be readily estimated from unpaired (or paired) samples of X and Y. Moreover, a great deal of the algorithmic complexity seen in the literature is motivated by issues which arise in high-dimensions (41), while our data is intrinsically one-dimensional.

Overview of the Algorithm

Given the experimentally determined discrete estimates $\mathbf{P_X}$ and $\mathbf{P_Y}$, we propose decomposing the problem of estimating f into two steps:

1. Finding a maximum a posteriori (MAP) discrete estimates of $P_{\bar{X}}$ and P_χ, which we denote $\hat{\mathbf{P}}_{\bar{\mathbf{X}}}$ and $\hat{\mathbf{P}}_\chi$, respectively. This may can be accomplished using the blind deconvolution algorithm (42). We note that it is also possible to do the same for $P_{\bar{Y}}$ and P_γ, but without the mapping f (or f^{-1}) it is unclear whether these estimates satisfy Eq. (S32).

2. We estimate f and P_γ by solving the minimization problem

$$\begin{cases} \min_{f,P_\gamma} & \mathrm{KL}\left(P_{\bar{Y}}\left(f\right) * P_\gamma \,|P_Y\right) + \lambda \mathrm{BV}\left(P_{\bar{Y}}\left(f\right)\right) \\ \text{subject to} & f' > 0,\ P_\gamma \geq 0\ \left\|P_\gamma\right\| = 1, \left\|\gamma P_\gamma\right\| = 0, \end{cases} \tag{S33}$$

where $\mathrm{KL}\left(p\,|q\right) = \int_{-\infty}^{\infty} p\left(x\right) \log\left(p\left(x\right)/q\left(x\right)\right) dx$ is the Kullback-Leibler Divergence, $P_{\bar{Y}}\left(f\right)$ is given by Eq. (S32), λ is a non-negative parameter, and $\mathrm{BV}\left(u\right) = \left\|u'\left(x\right)\right\|_2$ is a Tikhonov regularization term (43) which limits the irregularity of the estimate $P_{\bar{Y}}$. Here we have formally restricted our optimization to monotonically increasing functions ($f' > 0$), but we may also consider monotonically decreasing functions by substituting in the constraint $f' < 0$.

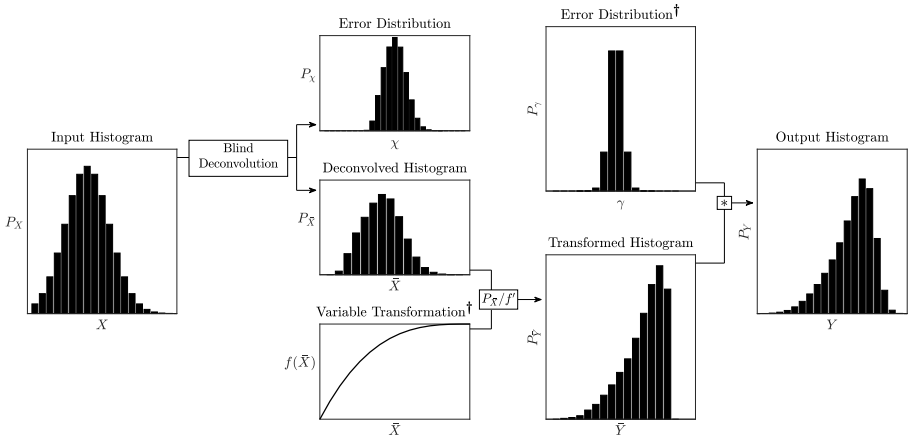

Figure S2: Schematic overview of the computational approach used to estimate P_Y given P_X, $f(\bar{X})$, and P_γ. The quantities that we seek to infer ($f(\bar{X})$ and P_γ) are marked with †.

Parametrization

Generally speaking, Bayesian inference methods, such as Markov Chain Monte Carlo (MCMC) techniques, produce samples of parameters θ, some of which may be used to estimate f. In this section, we detail our approach for reconstructing f from a given set of parameters θ. In the following section, we detail how to compare the experimental data $\mathbf{P_Y}$ to the model prediction $P_Y\left(\theta\right) = P_{\bar{Y}}\left(f\left(x\right)|\theta\right) * P_\gamma\left(\theta\right)$ in order to produce appropriate samples of θ.

A priori, we do not know what form the (possibly nonlinear) function f has, and thus we will assume only that it is continuous almost everywhere. Furthermore, from the problem specification (S33), the only constraint on the probability

density P_γ is that it must have zero mean, which is too weak of a constraint to justify using any specific parametric family of distributions. Therefore, we reconstruct both functions in a non-parametric manner. That is, f and P_γ are treated as discrete sets of values to be inferred using MCMC.

Let us denote the discrete ordered list of sample points for the histograms (i.e., bin centers) by

$$\mathbf{x} = [x_1, x_2, \ldots, x_M]$$

and

$$\mathbf{y} = \left[y_1, y_2, \ldots, y_Q\right]$$

such that $\mathbf{P_X} = P\left(X \in [\mathbf{x}, \mathbf{x} + dx]\right)$ and $\mathbf{P_Y} = P\left(Y \in \left[\mathbf{y}, \mathbf{y} + dy\right]\right)$. We aim to choose the parametrization of the function f in order to maximize the robustness of our computational approach. In order to do this, we take into account two intrinsic properties of our optimization problem. First, equation (S32) indicates that it is critical to know the derivative of f at the discrete values $\mathbf{x}$. Therefore, we choose to parametrize f primarily by its derivative rather than its value, which also allows for a straightforward means of constraining f to be a monotonic function as required by (S33). With an initial value f_1 for the function f, we may reconstruct f from its derivative using the fundamental theorem of calculus: $f(x) = f_1 + \int_{x_1}^{x} f'(s)\, ds$. Second, we aim to use the same parametrization for the entire class of monotonic functions, including both monotonically increasing and decreasing functions, that can be distinguished by the sign of $f_M - f_1$. In order to achieve both of these goals, we numerically reconstruct the discrete values of the function f from normalized samples of its derivative $\mathbf{f'}$, defined by $\boldsymbol{\phi} \coloneqq \mathbf{f'}/\left(f_M - f_1\right)$, where imposing $\boldsymbol{\phi} \geq 0$ guarantees monotonicity. Using this parametrization, f can be reconstructed using the formula $\mathbf{f}(\mathbf{x}) \coloneqq \mathbf{f}\left(\mathbf{x}\middle|f_1, f_M, \boldsymbol{\phi}\right) = f_1 + (f_M - f_1)\left[S_{\{1,\ldots,M\}}(\boldsymbol{\phi})\right]$, where

$$S_j(\mathbf{f'}) = \begin{cases} 0 & j = 1 \\ \sum_{i=1}^{j-1} \frac{f_i' + f_{i+1}'}{2}(x_{i+1} - x_i) & \text{otherwise} \end{cases}$$

is a trapezoidal approximation to the cumulative integral of f from x_1 to x_j. Furthermore, we may also compute the probability densities at $\bar{Y} = \mathbf{f}(\mathbf{x})$ using

$$\mathbf{P}_{\bar{\mathbf{Y}}}(\theta) \coloneqq \mathbf{P}\left(\bar{Y} = \mathbf{f}(\mathbf{x})\,|\theta\right) = \hat{\mathbf{P}}_{\bar{\mathbf{X}}}(\mathbf{x}) \oslash \left|\left(f_M - f_1\right)\boldsymbol{\phi}\right|,$$

where $\oslash$ denotes Hadamard division or the element-wise division of two vectors.

Bayesian Inference of the Transformation

In order to asses the validity of a given $(2 + M + Q)$-dimensional set of estimated parameters $\theta = [f_1, f_M, \boldsymbol{\phi}, \mathbf{P}_\gamma]$, we need to compare the discrete set of experimental measurements $\mathbf{P_Y}(\mathbf{y})$ with the estimated $\mathbf{P}\left(Y = \mathbf{f}(x)\,|\theta\right) \coloneqq \left(\mathbf{P}_{\bar{Y}} * \mathbf{P}_\gamma\right)$, a problem that is generally complicated by the fact that $\mathbf{y} \neq \mathbf{f}(\mathbf{x})$. To resolve this issue, we introduce an interpolant, given by

$$\tilde{P}_Y\left(y\,|\theta\right) = \begin{cases} \rho_i + \frac{\rho_{i+1} - \rho_i}{f_{i+1} - f_i}\left(y - f_i\right) & \text{if } \exists\, i : f_i < y \leq f_{i+1} \\ 0 & \text{otherwise} \end{cases},$$

where $\rho = \mathbf{P_Y}\left(\mathbf{f}(\mathbf{x})\,|\theta\right)$, allowing us to create a data-fidelity function for a given θ, given by

$$\Delta P(\theta) = \mathrm{KL}\left(\tilde{P}_Y\left(\mathbf{y}\,|\theta\right)|\mathbf{P_Y}\right).$$

Therefore, to solve problem (S33), we use the Gibbs sampler to sample θ from the posterior

$$\pi\left(\theta\,|\mathbf{P_Y}\right) \propto \mathcal{L}\left(\mathbf{P_Y}|\theta\right) Pr(\theta),$$

where $\mathcal{L}\left(\mathbf{P_Y}|\theta\right) = \exp\left[-\left(\Delta P(\theta) + \lambda BV\left(\mathbf{P}_{\bar{Y}}(\theta)\right)\right)\right]$ and $Pr(\theta)$ are the likelihood and prior densities of θ, respectively. Given the MAP estimate $\hat{\theta} = \left[\hat{f}_1, \hat{\mathbf{f}}', \hat{\mathbf{P}}_\gamma\right]$, we may readily obtain a MAP estimate of $\mathbf{f}$, using the formula

$$\hat{\mathbf{f}} = \mathbf{f}\left(\mathbf{x}\middle|\hat{f}_1, \hat{\mathbf{f}}'\right).$$

SUPPORTING REFERENCES

1. Rishita Changede and Michael Sheetz. "Integrin and cadherin clusters: A robust way to organize adhesions for cell mechanics". In: *BioEssays* 39.1 (2017), e201600123. ISSN: 02659247. DOI: 10.1002/bies.201600123. URL: http://doi.wiley.com/10.1002/bies.201600123.
2. Rishita Changede et al. "Nascent Integrin Adhesions Form on All Matrix Rigidities after Integrin Activation". In: *Developmental Cell* 35.5 (2015), pp. 614–621. ISSN: 15345807. DOI: 10.1016/j.devcel.2015.11.001. URL: http://www.ncbi.nlm.nih.gov/pubmed/26625956%20http://linkinghub.elsevier.com/retrieve/pii/S1534580715007157.
3. Olivier Rossier et al. "Integrins β 1 and β 3 exhibit distinct dynamic nanoscale organizations inside focal adhesions". In: *Nature Cell Biology* 14.10 (2012), pp. 1057–1067. ISSN: 14657392. DOI: 10.1038/ncb2588. URL: http://www.nature.com/articles/ncb2588.
4. Taka A. Tsunoyama et al. "Super-long single-molecule tracking reveals dynamic-anchorage-induced integrin function". In: *Nature Chemical Biology* 14.5 (2018), pp. 497–506. ISSN: 15524469. DOI: 10.1038/s41589-018-0032-5. URL: http://www.nature.com/articles/s41589-018-0032-5.
5. Alice Nicolas and Samuel A. Safran. "Limitation of cell adhesion by the elasticity of the extracellular matrix". In: *Biophysical Journal* 91.1 (2006), pp. 61–73. ISSN: 00063495. DOI: 10.1529/biophysj.105.077115. URL: http://www.ncbi.nlm.nih.gov/pubmed/16581840%20http://www.pubmedcentral.nih.gov/articlerender.fcgi?artid=PMC1479082.
6. Frederic Lagarrigue et al. "A RIAM/lamellipodin-talin-integrin complex forms the tip of sticky fingers that guide cell migration". In: *Nature Communications* 6 (2015), p. 8492. ISSN: 2041-1723. DOI: 10.1038/ncomms9492. URL: http://www.ncbi.nlm.nih.gov/pubmed/26419705%20http://www.pubmedcentral.nih.gov/articlerender.fcgi?artid=PMC4589889%20http://www.nature.com/doifinder/10.1038/ncomms9492.
7. Caroline Cluzel et al. "The mechanisms and dynamics of αvβ3 integrin clustering in living cells". In: *Journal of Cell Biology* 171.2 (2005), pp. 383–392. ISSN: 00219525. DOI: 10.1083/jcb.200503017. URL: http://www.ncbi.nlm.nih.gov/pubmed/16247034%20http://www.pubmedcentral.nih.gov/articlerender.fcgi?artid=PMC2171205.
8. S. E. Le Devedec et al. "The residence time of focal adhesion kinase (FAK) and paxillin at focal adhesions in renal epithelial cells is determined by adhesion size, strength and life cycle status". In: *Journal of Cell Science* 125.19 (2012), pp. 4498–4506. ISSN: 0021-9533. DOI: 10.1242/jcs.104273. arXiv: arXiv:0807.1760v1. URL: http://jcs.biologists.org/cgi/doi/10.1242/jcs.104273.
9. Michelle A Digman et al. "Paxillin dynamics measured during adhesion assembly and disassembly by correlation spectroscopy." In: *Biophysical journal* 94.7 (2008), pp. 2819–31. ISSN: 1542-0086. DOI: 10.1529/biophysj.107.104984. URL: http://www.sciencedirect.com/science/article/pii/S0006349508705332.
10. Haguy Wolfenson et al. "A role for the juxtamembrane cytoplasm in the molecular dynamics of focal adhesions". In: *PLoS ONE* 4.1 (2009), e4304. ISSN: 19326203. DOI: 10.1371/journal.pone.0004304. URL: http://www.ncbi.nlm.nih.gov/pubmed/19172999%20http://www.pubmedcentral.nih.gov/articlerender.fcgi?artid=PMC2627934.
11. Chi Li Chiu et al. "Nanoimaging of focal adhesion dynamics in 3D". In: *PLoS ONE* 9.6 (2014), e99896. ISSN: 19326203. DOI: 10.1371/journal.pone.0099896. URL: http://www.ncbi.nlm.nih.gov/pubmed/24959851%20http://www.pubmedcentral.nih.gov/articlerender.fcgi?artid=PMC4069057.
12. Yvonne Aratyn-Schaus and Margaret L Gardel. "Transient frictional slip between integrin and the ECM in focal adhesions under myosin II tension." In: *Current biology : CB* 20.13 (2010), pp. 1145–53. ISSN: 1879-0445. DOI: 10.1016/j.cub.2010.05.049. URL: http://www.ncbi.nlm.nih.gov/pubmed/20541412%20http://www.pubmedcentral.nih.gov/articlerender.fcgi?artid=PMC2902720.
13. D. P. Felsenfeld, D. Choquet, and M. P. Sheetz. "Ligand binding regulates the directed movement of β1 integrins on fibroblasts". In: *Nature* 383.6599 (1996), pp. 438–440. ISSN: 00280836. DOI: 10.1038/383438a0. URL: http://www.nature.com/doifinder/10.1038/383438a0.
14. Alice C. Chang et al. "Single Molecule Force Measurements in Living Cells Reveal a Minimally Tensioned Integrin State". In: *ACS Nano* 10.12 (2016), pp. 10745–10752. ISSN: 1936-0851. DOI: 10.1021/acsnano.6b03314. URL: http://pubs.acs.org/doi/abs/10.1021/acsnano.6b03314.
15. B. Ph Van Milligen et al. "On the applicability of Fick's law to diffusion in inhomogeneous systems". In: *European Journal of Physics* 26.5 (2005), pp. 913–925. ISSN: 01430807. DOI: 10.1088/0143-0807/26/5/023. URL: http://stacks.iop.org/0143-0807/26/i=5/a=023?key=crossref.18ae1d798b557c850b35a3b3bc9d721c.

16. P. F. Tupper and Xin Yang. “A paradox of state-dependent diffusion and how to resolve it”. In: *Proceedings of the Royal Society A: Mathematical, Physical and Engineering Sciences* 468.2148 (2012), pp. 3864–3881. ISSN: 14712946. DOI: 10.1098/rspa.2012.0259. arXiv: 1204.1590. URL: http://rspa.royalsocietypublishing.org/cgi/doi/10.1098/rspa.2012.0259.

17. R. L. Stratonovich. “Fokker-planck equation with discontinuous coefficients and conditions at the surface of discontinuity”. In: *Soviet Radiophysics* 8.4 (1965), pp. 500–505. ISSN: 00338443. DOI: 10.1007/BF01038325. URL: http://link.springer.com/10.1007/BF01038325.

18. A. Nicolas, B. Geiger, and S. A. Safran. “Cell mechanosensitivity controls the anisotropy of focal adhesions”. In: *Proceedings of the National Academy of Sciences* 101.34 (2004), pp. 12520–12525. ISSN: 0027-8424. DOI: 10.1073/pnas.0403539101. URL: http://www.pnas.org/cgi/doi/10.1073/pnas.0403539101.

19. Colin K Choi et al. “Actin and alpha-actinin orchestrate the assembly and maturation of nascent adhesions in a myosin II motor-independent manner.” In: *Nature cell biology* 10.9 (2008), pp. 1039–50. ISSN: 1465-7392. DOI: 10.1038/ncb1763. URL: http://www.ncbi.nlm.nih.gov/pubmed/19160484%20http://www.pubmedcentral.nih.gov/articlerender.fcgi?artid=PMC2827253.

20. Joseph E. Olberding et al. “The non-equilibrium thermodynamics and kinetics of focal adhesion dynamics”. In: *PLoS ONE* 5.8 (2010). Ed. by Markus J. Buehler, e12043. ISSN: 19326203. DOI: 10.1371/journal.pone.0012043. URL: http://dx.plos.org/10.1371/journal.pone.0012043.

21. Xuan Cao et al. “Multiscale model predicts increasing focal adhesion size with decreasing stiffness in fibrous matrices.” In: *Proceedings of the National Academy of Sciences of the United States of America* 114.23 (2017), E4549–E4555. ISSN: 1091-6490. DOI: 10.1073/pnas.1620486114. URL: http://www.ncbi.nlm.nih.gov/pubmed/28468803%20http://www.pubmedcentral.nih.gov/articlerender.fcgi?artid=PMC5468675.

22. Nir S Gov. “Modeling the size distribution of focal adhesions.” In: *Biophysical journal* 91.8 (2006), pp. 2844–7. ISSN: 0006-3495. DOI: 10.1529/biophysj.106.088484. URL: http://www.ncbi.nlm.nih.gov/pubmed/16861281%20http://www.pubmedcentral.nih.gov/articlerender.fcgi?artid=PMC1578473.

23. Zhenhai Li, Fang Kong, and Cheng Zhu. “A model for cyclic mechanical reinforcement”. In: *Scientific Reports* 6.1 (2016), p. 35954. ISSN: 2045-2322. DOI: 10.1038/srep35954. URL: http://www.nature.com/articles/srep35954.

24. Jing Li and Timothy A. Springer. “Integrin extension enables ultrasensitive regulation by cytoskeletal force”. In: *Proceedings of the National Academy of Sciences* 114.18 (2017), pp. 4685–4690. ISSN: 0027-8424. DOI: 10.1073/pnas.1704171114. URL: http://www.pnas.org/lookup/doi/10.1073/pnas.1704171114.

25. Yuriy V Pereverzev, Eugenia Prezhdo, and Evgeni V Sokurenko. “The two-pathway model of the biological catch-bond as a limit of the allosteric model.” In: *Biophysical journal* 101.8 (2011), pp. 2026–36. ISSN: 1542-0086. DOI: 10.1016/j.bpj.2011.09.005. URL: http://www.ncbi.nlm.nih.gov/pubmed/22004757%20http://www.pubmedcentral.nih.gov/articlerender.fcgi?artid=PMC3192973.

26. Fang Kong et al. “Demonstration of catch bonds between an integrin and its ligand”. In: *Journal of Cell Biology* 185.7 (2009), pp. 1275–84. ISSN: 1540-8140. DOI: 10.1083/jcb.200810002. URL: http://www.ncbi.nlm.nih.gov/pubmed/19564406%20http://www.pubmedcentral.nih.gov/articlerender.fcgi?artid=PMC2712956%20http://jcb.rupress.org/content/185/7/1275.

27. Peter Kloeden. *Numerical solution of stochastic differential equations*. Vol. 47. 1-2. Berlin, Heidelberg: Springer Berlin Heidelberg, 1994, pp. 121–126. ISBN: 978-3-642-08107-1. DOI: 10.1080/17442509408833885. arXiv: arXiv:1011.1669v3. URL: https://www.tandfonline.com/doi/full/10.1080/17442509408833885.

28. Christian L. Vestergaard and Mathieu Génois. “Temporal Gillespie Algorithm: Fast Simulation of Contagion Processes on Time-Varying Networks”. In: *PLoS Computational Biology* 11.10 (2015). Ed. by Marcel Salathé, e1004579. ISSN: 15537358. DOI: 10.1371/journal.pcbi.1004579. arXiv: 1504.01298. URL: https://dx.doi.org/10.1371/journal.pcbi.1004579.

29. C Ballestrem et al. “Marching at the front and dragging behind: differential alphaVbeta3-integrin turnover regulates focal adhesion behavior.” In: *The Journal of cell biology* 155.7 (2001), pp. 1319–32. ISSN: 0021-9525. DOI: 10.1083/jcb.200107107. URL: http://www.ncbi.nlm.nih.gov/pubmed/11756480%20http://www.pubmedcentral.nih.gov/articlerender.fcgi?artid=PMC2199321.

30. Kaixi Tang et al. “Paxillin phosphorylation at serine 273 and its effects on Rac, Rho and adhesion dynamics”. In: *PLoS Computational Biology* 14.7 (2018). Ed. by Anand R. Asthagiri, e1006303. ISSN: 15537358. DOI: 10.1371/journal.pcbi.1006303. URL: https://dx.plos.org/10.1371/journal.pcbi.1006303.

31. Fang Kong et al. “Cyclic Mechanical Reinforcement of Integrin Ligand Interactions”. In: *Molecular Cell* 49.6 (2013), pp. 1060–1068. ISSN: 10972765. DOI: 10.1016/j.molcel.2013.01.015. URL: http://www.ncbi.nlm.nih.gov/pubmed/23416109%20http://www.pubmedcentral.nih.gov/articlerender.fcgi?artid=PMC3615084%20http://linkinghub.elsevier.com/retrieve/pii/S1097276513000488.

32. Elisabetta Ada Cavalcanti-Adam et al. “Cell spreading and focal adhesion dynamics are regulated by spacing of integrin ligands.” In: *Biophysical journal* 92.8 (2007), pp. 2964–74. ISSN: 0006-3495. DOI: 10.1529/biophysj.106.089730. URL: http://www.ncbi.nlm.nih.gov/pubmed/17277192%20http://www.pubmedcentral.nih.gov/articlerender.fcgi?artid=PMC1831685.

33. Mark Schvartzman et al. “Nanolithographic Control of the Spatial Organization of Cellular Adhesion Receptors at the Single-Molecule Level”. In: *Nano Letters* 11.3 (2011), pp. 1306–1312. ISSN: 1530-6984. DOI: 10.1021/nl104378f. URL: http://www.ncbi.nlm.nih.gov/pubmed/21319842%20http://www.pubmedcentral.nih.gov/articlerender.fcgi?artid=PMC3061283%20https://pubs.acs.org/doi/10.1021/nl104378f.

34. Diederik P Kingma and Max Welling. *Auto-Encoding Variational Bayes*. Tech. rep. arXiv: 1312.6114v10. URL: https://arxiv.org/pdf/1312.6114.pdf.

35. Oren Rippel and Ryan Prescott Adams. *High-Dimensional Probability Estimation with Deep Density Models*. Tech. rep. 2013. arXiv: 1302.5125v1. URL: http://math.mit.edu/.

36. Laurent Dinh, Jascha Sohl-Dickstein, and Samy Bengio. “Density estimation using Real NVP”. In: *arXiv* arXiv (2016), p. 1605.08803v3. arXiv: 1605.08803. URL: https://arxiv.org/abs/1605.08803v3.

37. Pooyan Khajehpour Tadavani. *Nonlinear Dimensionality Reduction by Manifold Unfolding*. Tech. rep. URL: https://pdfs.semanticscholar.org/42ab/6c438bf5a6e0e74cc2dd9192a12f2406ca33.pdf.

38. S. Roberts et al. “Gaussian processes for time-series modelling”. In: *Philosophical Transactions of the Royal Society A: Mathematical, Physical and Engineering Sciences* 371.1984 (2012), pp. 20110550–20110550. ISSN: 1364-503X. DOI: 10.1098/rsta.2011.0550. URL: http://rsta.royalsocietypublishing.org/cgi/doi/10.1098/rsta.2011.0550.

39. Trevor Hastie and Robert Tibshirani. “Generalized additive models for medical research”. In: *Statistical Methods in Medical Research* 4.3 (1995), pp. 187–196. ISSN: 0962-2802. DOI: 10.1177/096228029500400302. URL: http://journals.sagepub.com/doi/10.1177/096228029500400302.

40. C E Rasmussen and C K I Williams. *Gaussian Processes for Machine Learning*. 1st ed. MIT Press, 2006, p. 248. ISBN: 026218253X. URL: www.GaussianProcess.org/gpml.

41. Sherjil Ozair and Yoshua Bengio. *Deep Directed Generative Autoencoders*. Tech. rep. arXiv: 1410.0630v1. URL: https://arxiv.org/pdf/1410.0630.pdf.

42. Daniele Perrone and Paolo Favaro. “A Clearer Picture of Total Variation Blind Deconvolution”. In: *IEEE Transactions on Pattern Analysis and Machine Intelligence* 38.6 (2016), pp. 1041–1055. ISSN: 0162-8828. DOI: 10.1109/TPAMI.2015.2477819. URL: http://ieeexplore.ieee.org/document/7254197/.

43. A. N. Tikhonov and Arsenin V. Y. *Solutions of ill-posed problems*. Winston, 1977, p. 258. ISBN: 0470991240.